PB82-259789

Techniques to Measure Volumetric Flow and Particulate Concentration in Stacks with Cyclonic Flow

Harmon Engineering and Testing
Auburn, AL

Prepared for

Environmental Monitoring Systems Lab.
Research Triangle Park, NC

Aug 82

U.S. Department of Commerce
National Technical Information Service
NTIS

PB82-259789

EPA-600/4-82-062
August 1982

TECHNIQUES TO MEASURE VOLUMETRIC FLOW AND PARTICULATE CONCENTRATION IN STACKS WITH CYCLONIC FLOW

by

J. Douglas Sterrett, Allen R. Barbin
Joe W. Reece, W. Glen Carter and
Bruce B. Ferguson
Harmon Engineering and Testing
1550 Pumphrey Avenue
Auburn, AL 36830

Task 2
EPA Contract No. 68-02-3215

Project Officer

William J. Mitchell
Quality Assurance Division (MD-77)
Environment Monitoring Systems Laboratory
Research Triangle Park, North Carolina 27711

ENVIRONMENTAL MONITORING SYSTEMS LABORATORY
OFFICE OF RESEARCH AND DEVELOPMENT
U.S. ENVIRONMENTAL PROTECTION AGENCY
RESEARCH TRIANGLE PARK, NC 27711

REPRODUCED BY
NATIONAL TECHNICAL
INFORMATION SERVICE
U.S. DEPARTMENT OF COMMERCE
SPRINGFIELD, VA 22161

TECHNICAL REPORT DATA
(Please read Instructions on the reverse before completing)

1. REPORT NO.	2.	3. RECIPIENT'S ACCESSION NO.
EPA 600/4-82-062		PB82 259789

4. TITLE AND SUBTITLE	5. REPORT DATE
TECHNIQUES TO MEASURE VOLUMETRIC FLOW AND PARTICULATE CONCENTRATION IN STACKS WITH CYCLONIC FLOW	August 1982
	6. PERFORMING ORGANIZATION CODE

7. AUTHOR(S)	8. PERFORMING ORGANIZATION REPORT NO.
J. Douglas Sterrett, Allen R. Barbin, Joe W. Reece, W. Glenn Carter and Bruce B. Ferguson	

9. PERFORMING ORGANIZATION NAME AND ADDRESS	10. PROGRAM ELEMENT NO.
Harmon Engineering and Testing, Inc. Auburn Industrial Park Auburn, AL 35810	11. CONTRACT/GRANT NO. 68-02-3215

12. SPONSORING AGENCY NAME AND ADDRESS	13. TYPE OF REPORT AND PERIOD COVERED
Environmental Monitoring Systems Laboratory Office of Research and Development U.S. Environmental Protection Agency Research Triangle Park, NC 27711	14. SPONSORING AGENCY CODE EPA 600/08

15. SUPPLEMENTARY NOTES

To be published as an ORD Project Report

16. ABSTRACT

The study determined that an in-stack venturi can accurately measure volumetric flow in stacks with a severe cyclonic flow profile. The design requirements of the venturi are described in the report. The report also describes a low head loss, egg crate-shaped device that effectively straightens cyclonic flow. Installation of such a device after a tangential inlet to a tall stack can result in considerable energy savings because it takes less fan power to push the straightened flow. Results to determine the particulate distribution downstream of the egg crate were inconclusive.

17. KEY WORDS AND DOCUMENT ANALYSIS

a. DESCRIPTORS	b. IDENTIFIERS/OPEN ENDED TERMS	c. COSATI Field/Group
In-stack venturi Flow straightener Egg crate straightener e´toile flow straightener Volumetric flow		

18. DISTRIBUTION STATEMENT	19. SECURITY CLASS *(This Report)*	21. NO. OF PAGES
RELEASE TO PUBLIC	UNCLASSIFIED	0
	20. SECURITY CLASS *(This page)* UNCLASSIFIED	22. PRICE

EPA Form 2220-1 (Rev. 4-77) PREVIOUS EDITION IS OBSOLETE

ABSTRACT

The ability of a venturi to measure volumetric flow in cyclonic flow situations was examined and a mathematical model describing the velocity field in the venturi throat was verified. As expected, the intensity of the swirling motion is magnified in the venturi throat, but an interesting acceleration of the core also occurs. In the cases examined, this acceleration produced a nearly uniform axial velocity profile in the venturi throat. Experimental results showed that the venturi can be calibrated to accurately measure volumetric flow even in the presence of a fairly strong swirling flow.

When differential equations of motion were solved for a variety of particle sizes and launch conditions, the results showed that the particulate concentration across the duct was not affected appreciably by the presence of the venturi in cyclonic flow situations.

Several straightening devices were evaluated to determine their ability to economically straighten swirling flow in stacks. It was found that egg crate assemblies with a cell length equal to or greater than the cell size were effective in straightening cyclonic flow with minimum head loss. It was also determined that using the egg crate assembly developed in this study in the breeching of tall stacks could result in significant energy savings compared to not straightening the flow. An empirical equation to predict the head loss for egg-crate assemblies was also developed.

A field study to determine the ability of the egg-crate assembly to redistribute the particulate in the stack gave inconclusive results.

CONTENTS

Abstract i
Figures iii
Tables vii
Abbreviations, Symbols and Metric Conversion Tables viii

1. Introduction 1
2. Conclusions 3
3. Recommendations 5
4. Phase I - Venturi Studies 6
   4.1 Flow model of swirling flow through the converging portion of a venturi 6
      4.1.1 Problem definition 6
      4.1.2 Flow model 7
      4.1.3 Analysis 7
      4.1.4 Sample Calculations 14
   4.2 Experimental facility and procedure 16
   4.3 Results and discussion 17
      4.3.1 Parametric head loss study 17
      4.3.2 Initial swirling flow data 18
      4.3.3 Additional swirling flow velocity profile data 19
      4.3.4 Duplication of initial data 20
      4.3.5 Fluid dynamics model -- correlation of initial data 20
      4.3.6 Computer processing of data 20
      4.3.7 Accuracy of the venturi as a volumetric flow measuring device 20
5. Phase II - Sampling for Particulate in Stacks with Cyclonic Flow 23
   5.1 Particulate behavior in cyclonic flow 23
   5.2 Wind tunnel studies on flow straighteners 27
   5.3 Results of wind tunnel studies 28
   5.4 Field evaluation of egg crate assembly 31

References 72
Appendix

A. Design and calibration of the inlet venturi 74

FIGURES

Number		Page
1	Definition sketch	33
2	Variation of transverse velocity	34
3	Stream tube in forced vortex core	34
4	Flow angle	34
5	Schematic of experimental facility	35
6	Flow measurement and regulation	36
7	Test section	37
8	Vane-type swirl generator	38
9	Tangential admittance swirl generator	39
10	Test venturi	40
11	Protractor-sampling block assembly	41
12	Frictional losses across a venturi	42
13	Axial velocity component at venturi entrance	43
14	Transverse velocity component at venturi entrance	43
15	Axial velocity component at venturi throat	43
16	Transverse velocity component at venturi throat	43
17	Axial velocity component at venturi exit	43
18	Transverse velocity component at venturi entrance	43
19	Axial velocity component at venturi entrance	44
20	Transverse velocity component at venturi entrance	44
21	Axial velocity component at venturi throat	44

22 Transverse velocity component at venturi throat 44

23 Axial velocity component at venturi exit 44

24 Transverse velocity component at venturi exit 44

25 Axial velocity component 5 ft downstream from venturi exit 45

26 Transverse velocity component 5 ft downstream from venturi exit 45

27 Axial velocity component 10 ft downstream from venturi exit 45

28 Transverse velocity component 10 ft downstream from venturi exit 45

29 Axial velocity component at venturi entrance 45

30 Transverse velocity component at venturi entrance 45

31 Axial velocity component at venturi throat 45

32 Transverse velocity component at venturi throat 46

33 Axial velocity component at venturi exit 46

34 Transverse velocity component at venturi exit 46

35 Transverse velocity, V_θ, simulation (approaching the venturi) 46

36 Axial velocity, V_Z, simulation (approaching the venturi). 46

37 Transverse velocity, V_θ, (calculated at throat) 46

38 Axial velocity, V_Z, (calculated at throat) 47

39 Percent change in discharge coefficient for orifice plate 48

40 Swirl correction factor C_D vs. swirl intensity m 48

41 Axial and tangential fluid velocities along stack radius for cyclonic flow 49

42 Radial particle velocities in cyclonic flow for particles starting at 70% of stack radius 49

43 Particle launch conditions in venturi throat (dashed line shows postulated trajectory) 50

44 Particle trajectories in venturi throat for 9.5° launch angle 51

45 Particle trajectories in venturi throat for 45° launch angle 51

46 Particle trajectories in venturi throat for 45° launch angle 51

47 D/4 egg crate-type flow straightener 52

48 8-vane étoile-type flow straightener 52

49 Schematic of experimental facility for straightener tests 53

50 Head loss vs. swirl intensity for a D/6 egg crate flow straightener (flow rate = 20 ft^3/s) 54

51 Head loss vs. swirl intensity for a D/6 egg crate flow straightener (flow rate = 30 ft^3/s) 55

52 Head loss vs. swirl intensity for a D/6 egg crate flow straightener (flow rate = 40 ft^3/s) 56

53 V_Z vs. locations of a D/6 egg crate flow straightener (length = 3 in, Q = 40 ft^3/s) 57

54 V_θ vs. location of a D/6 egg crate flow straightener (length = 3 in, Q = 40 ft^3/s) 58

55 Head loss vs. swirl intensity for egg crate-type flow straightener of cell size c = 4 1/2 in (flow rate = 40 ft^3/s) 59

56 V_Z vs. location for a D/4 egg crate flow straightener (length = 4 1/2 in, Q = 40 ft^3/s) 60

57 V_θ vs. location for a D/4 egg crate flow straightener (length = 4 1/2 in, Q = 40 ft^3/s) 61

58 Head loss vs. swirl intensity for a four vane étoile-type flow straightener (flow rate = 40 ft^3/s) 62

59 Head loss vs. swirl intensity for an eight vane étoile flow straightener (flow rate = 40 ft^3/s, straightener length = 36 in) 63

60 V_Z vs. location of four vane étoile flow straightener ($Q = 40\ ft^3/s$) 64

61 V_θ vs. location of four vane étoile flow straightener ($Q = 40\ ft^3/s$) 65

62 Total head loss vs. pipe L/D for straightened flow and swirling flow 66

TABLES

Number		Page
1	Core Velocity Profile at Throat	67
2	Experimental Results	68
3	Swirl Generator Calibration	69
4	Yaw Angles vs. Traverse Point	70
5	Comparison of Particulate Concentrations and Volumetric Flow Upstream and Downstream from the Egg Crate Straightener	71

ABBREVIATIONS, SYMBOLS AND METRIC CONVERSION FACTORS

SYMBOLS

a	-- acceleration
C_V	-- venturi discharge coefficient
C_D	-- venturi swirl discharge coefficient
D	-- diameter
$f()$	-- function of ()
L	-- length of diffuser
m	-- swirl intensity parameter
n	-- unit vector normal to control volume
p	-- pressure
ΔP	-- change in pressure
Q	-- volumetric flow rate
Q^*	-- volumetric flow rate in vortex sheath
R	-- pipe radius
t	-- time
T	-- temperature
V	-- velocity
β	-- diameter ratio ($D_{\text{venturi throat}}/D_{\text{duct}}$)
ε	-- unit vector, cylindrical coordinates
ρ	-- mass density
Θ	-- yaw angle
ϕ	-- pitch angle
δ	-- radius of forced vortex
Ω^*	-- angular momentum flux in free vortex
Σ	-- the summation of
$\equiv$	-- defined as

ABBREVIATIONS

$\mathcal{L}$	-- center line
ft^3/s	-- cubic feet per second
ft	-- feet
$^\delta F$	-- degree Fahrenheit
ft/s	-- feet per second
in	-- inch
R_e	-- Reynolds number
tan	-- trigonometric tangent

METRIC CONVERSION FACTORS

TO CONVERT	TO OBTAIN	MULTIPLY BY
feet	meters	0.3048
inches	centimeters	2.540
cubic feet	cubic meters	0.02832
slugs	kilograms	14.59
grams	milligrams	64.8

SECTION 1

INTRODUCTION

When cyclonic flow is present in stacks, it presents special problems in the measurement of pollutant concentration and emission rate, particularly for particulates and aerosols. These problems exist due to the nonuniformity of the cyclonic velocity profile across the stack and the tendency for any particulate matter to concentrate near the dust wall, where it is difficult to collect [1].

Reported here are the results of a study performed to evaluate the ability of a venturi to accurately measure volumetric flow in cyclonic flow situations and to determine if the use of an in-stack installed venturi would destroy the angular momentum vector as the gas passed through. If this occurred, the particulate concentrated near the wall by the cyclonic flow would be moved toward the center of the stack when the cyclonic flow patter was destroyed. This would both simplify sampling and improve the accuracy of the measurement while avoiding the problems of particulate loss associated with flow straightening devices. This study was divided into two phases.

The primary objectives of the first phase were:

1. Develop a mathematical model capable of predicting cyclonic flow velocity profiles in a venturi throat.

2. Validate the model in the laboratory.

3. Develop a model that would predict the particulate distributions in cyclonic flow and the effect of a venturi on these distributions.

4. Determine if the venturi can be used as a low-pressure-loss flow measuring device even in the presence of swirl flow.

When angular momentum was found to be conserved in the venturi and modeling demonstrated that the particulate would not be redistributed the second phase of this study was initiated to validate a means to effectively straighten flow with minimum head loss.

Thus, Phase II efforts were concentrated on developing a straightening vane that would have a low head loss and evaluating its ability to redistribute the particulate. In Phase II, the effectiveness of both egg crate and étoile flow straighteners was investigated

in wind tunnel tests for several different lengths and cell sizes to determine the smallest flow straightener that would effectively straighten cyclonic flow with minimum head loss. After wind tunnel tests were completed, a field evaluation was conducted at a fertilizer plant to evaluate the ability of the flow straightener developed in this study to redistribute the particulate.

SECTION 2

CONCLUSIONS

The following conclusions are drawn from this study:

1. The total pressure loss across an in-stack venturi will not be large, provided the venturi has been properly designed to prevent flow separation in the diffuser section.

2. For a given cyclonic flow situation, the throat velocity profile can be accurately predicted using the analytical model developed in this report.

3. An in-stack venturi does not straighten cyclonic flow. With the exception of a small amount of frictional decay, angular momentum, and hence swirl, is conserved in passing through a venturi. After passing through a venturi, the cyclonic flow profile is regenerated.

4. The characteristic region of low axial velocity in the center of a gas stream in cyclonic flow is accelerated in the venturi throat to give a nearly rectangular velocity profile in the venturi throat.

5. Flows with surprisingly high swirl rates ($m \leq 0.30$) can still be measured accurately with the venturi if the model developed in this study is used.

6. Calculated particulate distributions are not affected significantly by their transition through a venturi in swirling flow.

7. Some possible benefits of an in-stack installed venturi, designed according to the specifications developed in this study, can be:

   - Properly calibrated, a venturi can stand alone as a volume flow measuring device.

   - The axial velocity component in the venturi throat is nearly uniform across the cross section of the throat.

- The increased velocity in the venturi throat will make possible more accurate sampling in stacks with low velocities because most pitot tubes are inaccurate below 10 ft^3/s [1].

8. Swirling flow can be straightened with surprisingly small head loss using an egg crate straightener with a length that is equal to the cell size of the egg crate. Although this egg crate has the potential to move particulate which is near the stack wall back into the main part of the stack, the results of field tests designed to prove this were inconclusive.

SECTION 3

RECOMMENDATIONS

Based on this study, the following recommendations are made:

1. Additional swirling flow velocity field data should be taken in the venturi throat and in other locations in the duct by using the tangential admittance swirl generator. This would extend the venturi velocity profile data into the realm of very high swirl intensities. These additional data would also contribute to the understanding of the venturi flow rate signal when a strong swirl is encountered.

2. Analytical work should be done to find a simple measure of swirl intensity that can be used in determining the proper venturi swirl coefficient.

3. The low radial velocity components found in some of the swirling flow situations studied should be investigated further.

4. Additional data should be taken to establish correlations for venturi discharge coefficients as a function of the diameter ratio, β, and the swirl intensity.

5. Additional field testing should be conducted to establish the effect of the egg crate assembly on stack particulate distribution.

6. Plants with tall stacks with cyclonic flow might find it economically advantageous to straighten the flow at the stack entrance when the stack is not used as a particulate emissions control device. It would reduce energy costs and simultaneously make the velocity and particulate profile amenable to sampling with available methodology.

SECTION 4

PHASE I - VENTURI STUDIES

4.1 FLOW MODEL OF SWIRLING FLOW THROUGH THE CONVERGING PORTION OF A VENTURI

4.1.1 Problem Definition

We consider here the flow of a fluid with swirl through the converging section of the venturi shown in Figure 1. The conditions upstream of the venturi are taken as typical to those in swirling flow in long tubes, as reported by Senoo and Nagata [2]. Thus, at Station 1, upstream of the venturi, the swirl component of the flow is characterized by two regions:

1. An inner core of fluid where the θ-component of velocity varies linearly with radius (i.e., a forced vortex).

2. An outer sheath where V_θ varies inversely with radius (i.e., a free vortex).

$$V_{\theta 1} = \begin{cases} r_1 \omega_1 & 0 \le r_1 \le \delta_1 \\ k_1/r_1 & \delta_1 \le r_1 \le R_1 \end{cases}$$

The axial velocity distribution illustrated in Figure 1 is also typical of those measured by Senoo and Nagata at small-to-moderate swirl intensities. Thus, excluding the boundary layer effects at the pipe wall,

$$V_{z1} = \begin{cases} f(r_1) & 0 \le r_1 \le \delta_1 \\ V_{wz1} & \delta_1 \le r_1 \le R_1 \end{cases}$$

where the distribution $f(r_1)$ is considered to be given.

In the forced vortex core, the axial velocity can be considerably less than V_{wz}; indeed, under certain conditions, a region of backflow (negative axial velocity) may exist near the center line. This negative-velocity core has serious implications for stack sampling techniques. For example, besides the inherent inaccuracies involved

in measuring low velocities, the flow angles (with respect to axial lines) can be large with consequent errors introduced in isokinetic sampling procedures. Contraction of the flow via passage through a venturi, however, could alleviate some of these effects.

4.1.2 Flow Model

The flow in the converging nozzle is considered to consist of a forced vortex core and a free vortex sheath at each station along this length. Furthermore, the axial velocity in the sheath is assumed to be uniform; thus, the flow in the sheath is irrotational* so the Bernoulli equation can be applied between any two points in that portion of the flow.

The effects of friction on the flow in the nozzle are neglected, in as much as the flow is accelerated through the nozzle and is expected to respond primarily to pressure forces. Consistent with the frictionless assumption, the rotational core of the flow retains its identity (i.e., all the fluid particles in the forced vortex core at the throat have their origin in the forced vortex core in the approach flow); this follows from the fact that in a frictionless flow, vortex tubes are material tubes (Kelvin's theorem). It then follows that the free vortex sheath retains its identity also. The assumption of zero friction allows us to apply the Bernoulli equation between two points in the forced vortex core provided they are on the same streamline.

4.1.3 Analysis

Consider an axisymmetric flow in a circular tube with a variation of swirl velocity as illustrated in Figure 2. The radial component of Euler's equation of motion for this case is:

$$\frac{\partial p}{\partial r} = \rho \frac{V_\theta^2}{r} \qquad (1)$$

For the free vortex, $V_\theta = k/r$, and

$$\frac{\partial p}{\partial r} = \rho \frac{k^2}{r^3}$$

---

* Without rotation at any point in the flow field.

Thus

$$p = -\frac{\rho k^2}{2 r^2} + \rho c^*$$

or

$$\frac{p}{\rho} + \frac{V_\theta^2}{2} = c^* \quad (\delta \le r \le R) \tag{2}$$

in the free vortex.

In the forced vortex core, $V_\theta = r\omega$, and Equation 1 becomes,

$$\frac{\partial p}{\partial r} = \rho r \omega^2$$

Thus,

$$p = \frac{\rho}{2} r^2 \omega^2 + \rho c^{**}$$

or

$$\frac{p}{\rho} - \frac{V_\theta^2}{2} = c^{**} \quad (0 \le r \le \delta_1) \tag{3}$$

in the forced vortex. Constants c^* and c^{**} in Equations 2 and 3 are related by matching pressures from the two equations. Thus,

$$\frac{p(\delta)}{\rho} = c^* - \frac{(k/\delta)^2}{2} = c^{**} + \frac{(\delta\omega)^2}{2}$$

Therefore,

$$c^* = c^{**} + 1/2(\delta^2\omega^2 + k^2/\delta^2) \tag{4}$$

Also, a velocity match at $r = \delta$ shows that

$$k/\delta = \delta\omega$$

or

$$k = \delta^2\omega \tag{5}$$

Equation 4 can thus be written as

$$c^* = c^{**} + \delta^2\omega^2 \tag{6}$$

The constant c^* can be evaluated at $r = R$ (pipe radius) as

$$c^* = \frac{p_w}{\rho} + \frac{V_{\theta w}}{2} \tag{7}$$

where "w" designates a "wall" value. From Equation 6, c^{**} is thus evaluated as

$$c^{**} = \frac{p_w}{\rho} + \frac{V_{\theta w}^2}{2} - \delta^2\omega^2 = \frac{p_w}{\rho} + \frac{k^2}{2R^2} - \delta^2\omega^2 \tag{8}$$

To apply Bernoulli's equation in the core, we need to locate two points on the same streamline. Consider an annular stream tube between two sections, designated by subscripts 1 and 2 (Figure 3). The volume flow rate past Section 1 is equal to that past Section 2; thus

$$2\pi V_{z1} r_1 \delta r_1 = 2\pi V_{z2} r_2 \delta r_2 \tag{9}$$

Also, since shear is zero, the angular momentum entering the stream-tube is identical to that leaving; thus

$$2\pi\rho V_{z1} V_{\theta 1} r_1^2 \delta r_1 = 2\pi\rho V_{z2} V_{\theta 2} r_2^2 \delta r_2 \tag{10}$$

If Equations 9 and 10 are divided, there results

$$V_{\theta 1}\, r_1 = V_{\theta 2}\, r_2$$

or

$$r_1^2\, \omega_1 = r_2^2\, \omega_2 \tag{11}$$

Thus, a particle at radius r_2 at Station 2 lies on a streamline which, at Station 1, passes through the radius r_1

$$r_1 = r_2 \left[{}^{\omega_2}/_{\omega_1} \right]^{1/2} \tag{12}$$

The volume flow in the free vortex sheath, Q^*, is

$$Q^* = \int_{\delta}^{R} 2\pi V_z\, r\, dr = \pi R^2 V_{zw} \left[1 - ({}^{\delta}/_{R})^2 \right] \tag{13}$$

The angular momentum flux in the free vortex sheath, Ω^*, is

$$\Omega^* = \int_{\delta}^{R} 2\pi V_\theta V_z\, r^2\, dr = \pi k V_{zw} R^2 \left[1 - ({}^{\delta}/_{R})^2 \right] \tag{14}$$

From Equations 13 and 14,

$$\frac{\Omega^*}{Q^*} = k \tag{15}$$

Since the volume flow rate and the angular momentum flux in the free vortex sheath remain constant in the venturi, Equation 15 shows that the parameter k also remains constant. Thus,

$$k_1 = k_2 = k \tag{16}$$

Equations 16 and 13 can be utilized to calculate the wall velocity components at the throat of the nozzle, Station 2, to wit,

$$V_{\theta w 2} = {}^{k_2}/_{R_2} = {}^{k}/_{R_2} \tag{17}$$

$$V_{zw2} = V_{zw1} \left[\frac{R_1^2 - \delta_1^2}{R_2^2 - \delta_2^2} \right] \tag{18}$$

As mentioned previously, we can apply the Bernoulli equation between two points in the forced vortex core, provided the points lie in the same streamline. Thus,

$$\frac{p(r_1)}{\rho} + \frac{V_{z1}^2(r_1) + r_1^2\omega_1^2}{2} = \frac{p(r_2)}{\rho} + \frac{V_{z2}^2(r_2) + r_2^2\omega_2^2}{2} \qquad (19)$$

where

$$r_1 = r_2\left[\omega_2/\omega_1\right]^{1/2}$$

Utilizing Equation 3, we can simplify Equation 19 as follows:

$$c_1^{**} + r_1\omega_1^2 + \frac{V_{z1}^2(r_1)}{2} = c_2^{**} + r_2\omega_2^2 + \frac{V_{z2}^2(r_2)}{2}$$

or

$$V_{z2}(r_2) = \left[V_{z1}^2\left(r_2\left[\omega_2/\omega_1\right]^{1/2}\right) + 2\left[(c_1^{**} - c_2^{**}) + r_1^2\omega_1^2 - r_2^2\omega_2^2\right]\right]^{1/2} \qquad (20)$$

From Equation 11, $r_1^2\omega_1 = r_2^2\omega_2$. Thus, Equation 20 can be written as

$$V_{z2}(r_2) = \left[V_{z1}^2\left(r_2\left[\omega_2/\omega_1\right]^{1/2}\right) + 2\left[(c_1^{**} - c_2^{**}) + r_2^2\omega_2(\omega_1 - \omega_2)\right]\right]^{1/2} \qquad (21)$$

From Equation 8,

$$c_1^{**} - c_2^{**} = \left(\frac{p_{w1}}{\rho} + \frac{V_{\theta w1}}{2} - \delta_1^2\omega_1^2\right) - \left(\frac{p_{wz}}{\rho} + \frac{V_{\theta w2}^2}{2} - \delta_2^2\omega_2\right) \qquad (22)$$

The Bernoulli equation in the free vortex sheath is

$$\frac{p_{w1}}{\rho} + \frac{V_{\theta w1}^2 + V_{zw1}^2}{2} = \frac{p_{w2}}{\rho} + \frac{V_{\theta w2}^2 + V_{zw2}^2}{2} \tag{23}$$

Combination of Equations 22 and 23 yields the expression for $c_1^{**} - c_2^{**}$

$$c_1^{**} - c_2^{**} = \frac{V_{wz1}^2}{2} - \delta_1^2\omega_1^2 - \frac{V_{wz2}^2}{2} + \delta_2^2\omega_2^2$$

which can be substituted in Equation 21 to yield

$$V_{z2}(r_2) = \left[V_{z1}^2 \left(r_2 \left[\omega_2/\omega_1 \right]^{1/2} \right) + V_{wz2}^2 - V_{wz1}^2 + 2\left[r_2^2\omega_2(\omega_1 - \omega_2) - \delta_1^2\omega_1^2 + \delta_2^2\omega_2^2 \right] \right]^{1/2} \tag{24}$$

Equation 24 can be simplified using equations 5 and 16. Thus,

$$V_{z2}(r_2) = \left[V_{z1}^2 \left(r_2 \frac{\delta_2}{\delta_1} \right) + V_{wz2}^2 - V_{wz2}^2 + 2k^2 \left(\frac{1}{\delta_2^2} - \frac{1}{\delta_1^2} \right) \left(1 - r_2^2/\delta_2^2 \right) \right]^{1/2} \qquad 0 \le r_2 \le \delta_2 \tag{25}$$

Solution of Equation 25 requires δ_2, the core radius at Station 2. δ_2 is not calculated directly; it must be so selected that the velocity profile calculated from Equation 25 yields the correct volume flow rate in the core

$$Q^{**} = \int_0^{\delta_2} 2\pi V_{z2} r_2 \, dr_2 = \int_0^{\delta_1} 2\pi V_{z1} r_1 \, dr_1$$

or

$$\int_0^{\delta_2} V_{z2} r_2 \, dr_2 = \int_0^{\delta_1} V_{z1} r_1 \, dr_1 = \frac{Q^{**}}{2\pi} \tag{26}$$

Calculation of the velocity profile at the venturi throat is based on Equations 18, 25 and 26. Given conditions at the upstream Station 1 (V_{wz1}, V_{z1}, k, R_1, δ_1), a value of δ_2 is assumed, Equation 18 is used to calculate V_{wz2} and Equation 25 is utilized to calculate the velocity profile in the core, $V_{z2}(r_2)$, $0 \leq r_2 \leq \delta_2$. Closure is based on Equation 26. If the calculated velocity profile, $V_{z2}(r_2)$, does not yield the correct flow through the core, a new value of δ_2 is assumed and the procedure is repeated until Equation 26 is satisfied.

Nondimensional forms of Equations 18, 25 and 26 can be expressed (with some manipulation) as

$$V'_{z2}(\xi_2) = \left\{ \beta^2 \left[V'^2_{z1}(\xi_2) - 1 \right] + 1 + 2\beta^2 (\tan^2 \theta_1^*) \left[\frac{\delta_1'^2}{\delta_2'^2} \left(R_1/R_2 \right)^2 - 1 \right] (1 - \xi_2^2) \right\}^{1/2} \qquad (25)'$$

$$\frac{\delta_2'^2}{\beta} \int_0^1 V'_{z2}(\xi)\, \xi d\xi = \delta_1'^2 \left(R_1/R_2 \right)^2 \int_0^1 V'_{z1}(\xi)\, \xi d\xi \qquad (26)'$$

Where

$$V'_{z1} \equiv V_{z1}/V_{wz1} \qquad (27)$$

$$V'_{z2} \equiv V_{z2}/V_{wz2} \qquad (28)$$

$$\beta \equiv \left(R_2/R_1 \right)^2 \left[\frac{1 - \delta_2'^2}{1 - \delta_1'^2} \right] = \frac{V_{wz1}}{V_{wz2}} \qquad (18)'$$

$$\delta_1' \equiv {}^{\delta_1}/_{R_1}, \tag{29}$$

$$\delta_2' \equiv {}^{\delta_2}/_{R_2}, \tag{30}$$

$$\xi \equiv {}^{r}/_{\delta}, \tag{31}$$

The angle θ_1 is the flow angle (yaw angle), measured in the z - θ plane at $r_1 = {}_1$ (Figure 4).

4.1.4 Sample Calculations

To illustrate the effect of contraction in the venturi throat on the velocity profile, an upstream approach flow with the following conditions is assumed**

$$R_1 = 3 \text{ ft.}$$

$$V_{wz1} = 50 \text{ fps}$$

$$\delta_1 = 1 \text{ ft.}$$

$$V_{z1} = \begin{cases} 10 + 40\, r_1, \text{ fps} & 0 \leq r_1 \leq 1 \text{ ft.} \\ 50 \text{ fps} & 1 \text{ ft.} \leq r_1 \leq 3 \text{ ft.} \end{cases}$$

$$\theta_1^* = 31.8^\circ$$

The radius of the venturi throat is taken to be

$$R_2 = 1.5 \text{ ft.}$$

** English units of measure are used in this report to reflect current practice in aerodynamic measurements. The English units can be converted to metric system units using the table on page vi of this report.

For these conditions and an assumed upstream core radius of

$$\delta_2 = 0.426 \text{ ft. (assumed)}$$

Equations (18)' and (25)' become (at the venturi throat)

$$\beta = 0.259 = \frac{V_{wz1}}{V_{wz2}} \qquad (18)'$$

$$V'_{z2} = \left[0.0671 \left[V'^{2}_{z1} (\xi_z) - 1\right] + 1 + 0.23274(1 - \xi_2^2)\right]^{1/2} \qquad (25)'$$

or

$$V'_{z2} = \left[1.1683191 + 0.021472\ \xi_2 - 0.1897911\ \xi_2^2\right]^{1/2} \qquad (32)$$

The axial velocity profile in the core, as calculated with Equation 32 is listed in Table 1. Using the values in Table 1 numerical integration yields:

$$\frac{\delta'^2_2}{\beta} \int_0^1 V'_{z2}(\xi)\, \xi d\xi = \frac{1}{0.259} \left(\frac{0.426}{1.5}\right) (0.5211) = 0.16228 \qquad (33)$$

whereas

$$\delta'^2_1 \left(R_1/R_2\right)^2 \int_0^1 V'_{z1}(\xi)\, \xi d\xi = \delta'^2_1 \left(R_1/R_2\right)^2 \int_0^1 (0.2 + 0.8\xi)\, \xi d\xi$$

$$= \delta'^2_1 \left(R_1/R_2\right)^2 \left[\frac{0.2}{2} + \frac{0.8}{3}\right] = \left(\frac{1}{3}\right)^2 \left(\frac{3}{1.5}\right)^2 (0.36667)$$

$$= 0.16296 \qquad (34)$$

Equations 33 and 34 show that Equation (26)' is satisfied (to within 4%), and no further iteration is required.

4.2 EXPERIMENTAL FACILITY AND PROCEDURE

The test facility used to validate the mathematical model in this investigation is shown in Figure 5. The section on the suction side of the fan, Figure 6, contains an adjustable flow regulating cone, straightening vanes, and a venturi calibrated to measure the incoming flow rate (see Appendix A).

The section on the downstream side of the fan is the test section containing the swirl generator, test venturi, and sampling stations. A basic duct diameter of 18 in. was chosen for this section and fabrication was made in lengths of from 2.5 to 10 ft. Each section of the pipe was flanged and gasketed to allow quick rearrangement of the test facility. The total assembled length of this section is approximately 40 ft., or 26.7 pipe diameters. A typical setup of the test section is shown in Figure 7.

Some of the test section components are described below.

Vane Type Swirl Generator (Figure 8): The vane-type swirl generator consists of eight sheet metal vanes mounted between two rings on threaded shafts. The inner ring is a section of 2-in. pipe while the outer ring is a plywood laminate 1.5 in. thick with an inner diameter of 18 inches. The eight shafts were externally linked together to provide external articulation of all the vanes.

Tangential Admittance Swirl Generator (Figure 9): The high intensity swirl generator was used only in gathering data for the venturi flow signal experiment. It is comprised of a 4x4x8 ft. plenum chamber which cascades air into the test section through four 24x4 in. longitudinal slots. Hinged vanes, located in these slots, are externally articulated by use of a belt pully system. This device generates very intense swirling flows, with yaw angles up to 105° (backflow) having been measured.

Test Venturi (Figure 10): This conical venturi has an inlet diameter of 18 in. and a throat diameter of 12 in., yielding a diameter ratio of .66. This device was fabricated in two sections, the converging-throat section and the diffuser section. These sections are flanged to allow insertion of sampling apparatus in the venturi throat. The venturi converges in one pipe diameter yielding a total included angle of 18.4°. The diffuser section is two pipe diameters in length with a total included angle of 9.5°. Six equally spaced pressure taps are located at the venturi throat and connected to a common header.

Sampling Apparatus: The sampling probe chosen was a United Sensors® DA-375 three dimensional directional probe. The device was capable of measuring both the yaw and pitch angles of the flow, as well as the total and static pressures of the fluid at the sampling point.

The protractor-block assembly, Figure 11, was designed to measure the yaw angle when the probe was aligned with the tangential flow vector. Later, a magnetic based protracter with a bubble level was used for this purpose.

The following procedure was followed during each of the test runs:

1. The sampling probe was moved to the traverse station and the protractor was "zeroed".

2. The desired swirl intensity was set by adjusting the swirl generator vane control linkage.

3. The inlet cone was adjusted to the desired flow rate and the pressure drop across the inlet venturi was recorded.

4. A quick traverse was made with the velocity probe to assure that a symmetrical flow field was being generated.

5. The probe was returned to the first sampling point and rotated (yawed) until it aligned with the flow, the manometer readings were recorded.

6. The probe was then moved to the next point on the traverse, rotated until aligned with the flow and the manometer readings recorded. This procedure was repeated at all points on the traverse.

7. After the entire traverse was completed, the pressure drop across the test venturi was recorded, and the pressure drop across the inlet venturi was rechecked.

4.3 RESULTS AND DISCUSSION

4.3.1 Parametric Head Loss Study

Parametric calculations show that the total pressure loss across an in-stack venturi is not very great, provided that the diffuser section has been designed to prevent flow separation; i.e., the gas

streamlines do not leave the wall and form an asymmetric flow in the diffuser. The values for physical constants, expansion coefficients, and friction factors were taken from references [3] and [4].

Figure 12 shows the results of a sample calculation of pressure loss versus inlet velocity for a venturi with an inlet-to-throat, diameter ratio (β) of 0.66. The stack gas temperature is taken to be 300°F and the mass density is assumed to be equivalent to that of air. In all calculations, the length of the converging section of the venturi is one inlet diameter. The third parameter used is the length of the diffuser length over the inlet diameter.

The optimum length for the diffuser section is found when the pressure loss is at a minimum. In Figure 12 this point is reached when the diffuser section has a length of 2.5 inlet diameters. Beyond this point, the frictional losses overcome the diffuser pressure recovery and the total pressure loss starts to increase.

4.3.2 Initial Swirling Flow Data

The results, reported in Figures 13 through 18, were obtained with the test facility arrangement shown in Figure 5. Velocity data were taken at 1/2-in. intervals across a pipe diameter.

Figures 13 and 14 show V_z and V_θ as functions of the pipe radius at the entrance plane of the venturi. These figures show a classical swirling profile[2], characterized by a center region of very low axial velocity.

Of obvious interest is the question: "How do these profiles compare with those found in the throat of the venturi?"

Figures 15 and 16 show V_z and V_θ as functions of the throat radius. It can be seen here that the axial component of velocity has been greatly increased in the center region (from what may have been actual backflow) to a nearly rectangular profile.

The data taken at the venturi exit plane is reported in Figures 17 and 18. These data were taken to see if the character of the swirl had been altered by passage through the venturi. The transverse velocity component, V_θ, is still much in evidence but the axial component of velocity has been altered drastically.

Numerical integrations of the axial velocity profiles were performed to obtain the flow rate in the pipe. For example,

$$Q(\text{cfs}) = \sum_{i=1}^{n} 2\pi r_i \Delta r V_{zi} \tag{35}$$

The results were:

$$Q_{entrance} = 24.16 \text{ ft}^3/\text{s}$$
$$Q_{throat} = 24.33 \text{ ft}^3/\text{s}$$
$$Q_{exit} = 24.58 \text{ ft}^3/\text{s}$$

These results are very close to the flow rate indicated by the flow measuring venturi, which validates the continuity equation.

4.3.3 Additional Swirling Flow Velocity Profile Data

The data shown in Figures 19 through 28 were taken at a flow rate of about 28 ft^3/s with the test venturi positioned as shown in Figure 5.

The data reported in Figures 19 through 24 were taken at the entrance, throat, and exit planes of the test venturi. Each figure shows three velocity profiles, representing each of three different swirl intensities. These three intensities were generated by changing the swirl generator blade angle from full angle to 3/4 to 1/2 of the maximum swirl generator blade angle. These three positions are shown by [S], (S), and (S), respectively.

These profiles are very similar in form to those reported above, however, the character of the axial velocity profile in the venturi throat is still of particular interest. For example, note that for each of the swirl intensities, the center section velocity has been increased to yield a nearly rectangular profile.

Figures 25 through 28 are representative of the data taken at locations 5 and 10 ft. downstream of the venturi exit plane (points ① and ② on Figure 5). Of interest here is the character of the axial velocity profile downstream from the venturi. The figures show a deceleration taking place in the center region of flow until a profile similar to that found at the venturi entrance is reached.

In general, the air enters the venturi with the classical profile of swirling flow. In the venturi throat, the flow has been accelerated to yield a nearly rectangualr profile for the axial velocity component. In leaving the venturi, this axial profile is still somewhat rectangular, but in moving downstream it reverts back to its original form.

On the other hand, the transverse velocity profiles, V_θ, show only a slight decay as the flow proceeds downstream. This decay is due to friction and appears to be little affected by the venturi.

4.3.4 Duplication of Initial Data

The same conditions resulting in the initial data were duplicated to see if the alterations of the velocity profiles by the test venturi were correct. These duplication data are shown, by Ⓢ, on Figures 29 through 34 along with the initial data. Although the flow rate was allowed to decrease by about 5% during the sampling period, the results are very similar. The repeatability of the initial data thus lends credence to the experimental results obtained in this study.

4.3.5 Fluid Dynamics Model--Correlation to Initial Data

The analytical model developed in Section 4.1 was used to predict the effect of the venturi on swirling flow velocity profiles. The model is based on the assumption that the swirling flow approaching the venturi is composed of a forced vortex core with a free vortex sheath filling the outer portion of the pipe [2]. The experimental data confirm that the flow present in the experiments does have this character. Figure 35 shows the data, V_θ, for a typical case with the vortex combination simulation. Figure 36 shows the accompanying axial component of velocity, V_z. The simulated velocity profiles are represented by solid lines and the s are the initial data points. These two velocity profiles, then, comprise the "input" for the mathematical model.

Figure 37 shows that the model predicts correctly the transverse velocity magnification in the venturi throat. Figure 38 shows that the model also correctly predicts the axial acceleration of the core portion of the flow. We are unaware of any previously published model that would predict these results for the axial acceleration and allow calculation of both the transverse and axial velocity profiles.

4.3.6 Computer Processing of Data

A computer program was developed to reduce the United Sensors® three-dimensional directional probe readings into orthogonal velocity components. A great deal of time was required to reduce these readings by hand, thus dictating the need for computer processing.

4.3.7 Accuracy of the Venturi as a Volumetric Flow Measuring Device

The objective of the work reported in this section was to determine whether the presence of swirl causes a change in the differential pressure indicated by a venturi flow meter.

For correlative purposes it is desired to use the swirl "strength" parameter, m. This parameter has been used by researchers studying the effect of swirling flow on the accuracy of an orifice

plate meter [7], and in a previous preliminary study on the accuracy of a venturi meter [8]. It also has been used in a study of swirling flow decay in long pipes with different roughnesses [2].

The integral form of m is,

$$m = \frac{2\pi\rho \int_0^R V_z V_\theta r^2 dr}{\left[2\pi\rho \int_0^R V_z^2 r dr\right] \times R} \tag{36}$$

where,

ρ = .00238 (slugs/ft^3 for air),
V_z = velocity in the axial direction (ft/s),
V_θ = velocity in the transverse direction (ft/s),
r = radial coordinate (in),
R = radius of duct = 9 in.

A numerical integration form of this swirl parameter is,

$$m = \frac{2\pi\rho \sum_{i=1}^{n} (V_{zi} V_{\theta i}) r_i^2 \Delta r}{\left[2\pi\rho \sum_{i=1}^{n} (V_{zi}^2 r_i) \Delta r\right] \times R} \tag{37}$$

where,

n = number of elements used to cover the flow area.

In terms of angular and axial momentum fluxes, this swirl parameter is seen to be

$$m = \frac{\text{angular momentum flux}}{\text{axial momentum flux} \times R} \tag{38}$$

For the range of swirl strengths achieved in the experiments [8], ($0.234<m<0.364$), there was no observed effect on the swirling flow signal; i.e., these results indicate that the venturi ΔP will allow an accurate flow rate calculation even for swirling flow up to m = 0.30.

For an orifice plate, the work reported in Reference 7 shows that the orifice plate flow signal was affected at m = 0.36 by about 5% for

$\beta = D_{throat}/D_{duct}$ of 0.66 (Figure 39).

The data reported in this section are the results of 26 velocity traverses, representing different settings on the tangential admittance swirl generator (Figure 9) and different volumetric flow rates.

The volumetric flow rates were calculated by the use of the continuity equation and Bernoulli's equation. The ideal volumetric flow rate is,

$$Q_{ideal} = VA \tag{39}$$

so therefore,

$$Q_{ideal} = \left[\frac{2\Delta P}{\rho\left[\left(\frac{D_1}{D_2}\right)^4 - 1\right]}\right]^{\frac{1}{2}} \left(\frac{\pi D_1^2}{4}\right) \tag{40}$$

where,

D_1 = diameter of entrance of venturi (in.)
D_2 = diameter of throat of venturi (in.)

For each case, $Q_{actual} = C_v Q_{ideal}$, since this is the manner in which the venturis were calibrated. All of the approach and discharge factors are incorporated into the venturi coefficient, C_v. By use of the Reynolds number and the velocity coefficient curve for each venturi, the C_v for the inlet venturi (venturi upstream of fan) and the test venturi was determined.

The actual volumetric flow rate found at the inlet venturi with no swirl present divided by the actual volumetric flow rate found at the test venturi with swirl present is defined as C_D, the venturi swirl discharge coefficient.

The end product of this work is displayed in Table 2, and in Figure 40 as a plot of the venturi swirl discharge coefficient, C_D, versus the swirl intensity, m.

The results of this study show that high intensity swirl ($m>0.30$) has a definite effect on the accuracy of a venturi as a volumetric flow measuring device. The results also show that for high intensity swirl there can be a region of backflow near the center line. This region of backflow, coupled with the combined effects of unusual pressure fields due to the swirling flow, cause the venturi inaccuracy. Measurements made have allowed a swirl correction coefficient versus swirl intensity relation to be deduced.

SECTION 5

PHASE II. SAMPLING FOR PARTICULATE IN STACKS WITH CYCLONIC FLOW

5.1 PARTICULATE BEHAVIOR IN CYCLONIC FLOW

Theoretical and experimental studies [9-11] have shown that in stacks with cyclonic flow much of the particulate is rapidly convected outward towards the wall and tends to remain there as it moves up the stack. For example, Peeler, et al, [10] showed that particulates 25 microns and larger in diameter will fairly quickly be flung radially outward toward the pipe wall by a cyclonic flow characterized by the velocity profiles shown in Figure 41. Their analysis proceeded with the assumption that the particles would be moving with the rotating gas flow as far as the transverse and axial velocity components were concerned. The ensuing trajectories of the particles were obtained with the assumption that they were "launched" with no radial velocity component, but with the gas velocity in Z and θ directions where the velocity vector is

$$\vec{V} = V_r\hat{\varepsilon}_r + V_\theta\hat{\varepsilon}_\theta + V_z\hat{\varepsilon}_z \qquad (41)$$

All particles were so launched at $r = 0.7R_o$ and their progress toward the wall was calculated. Figure 42 shows how the particles acquire radial speed as they move toward the wall.

The problem to be solved in the case of cyclonic flow entering the throat of a venturi differs from that considered by Peeler et. al. [10] in that the particles must be "launched" with an inward velocity component. Figure 43 shows the initial conditions. The dashed line shows the theoretical particle trajectory with respect to its radial movement. It should be remembered that the trajectory is actually a spiral with a varying radius. The initial or "launch" velocity is $\vec{V}_o$ and its radial component, V_{ro}, is dictated by the venturi angle, θ, and the average axial velocity, $\bar{V}_z$. Recall that the axial velocity is accelerated by the venturi to yield an almost rectangular profile (see, for example, Figure 15). The radial launch velocity is

$$V_{ro} = -\bar{V}_z \tan\theta \qquad (42)$$

In order to compare the results obtained for this problem with those obtained by Peeler et. al. [10] the particles will all be launched at $r = 0.7R_o$ and velocity components similar to those shown in Figure 41 will be used.

A brief account of the modeling technique follows. The position vector of a particle is given by

$$\vec{r} = r\hat{\varepsilon}_r + Z\hat{\varepsilon}_z \tag{43}$$

and its velocity is expressed as in Equation 41. The particle's acceleration components in the r and θ directions are

$$a_r = \frac{d^2r}{dt^2} - r\left(\frac{d\theta}{dt}\right)^2 \tag{44}$$

and

$$a_\theta = r\frac{d^2\theta}{dt^2} + 2\frac{dr}{dt}\frac{d\theta}{dt} \tag{45}$$

Since it is assumed that the particle is transported with the fluid in the transverse direction, there are no transverse viscous forces on the particle and $a_\theta = 0$. This results in the classical case of conservation of angular momentum or

$$V_\theta r = \text{constant} = C \tag{46}$$

Movement of the particle relative to the fluid in the radial direction results, however, in a viscous drag force. Because the relative radial velocity is not great and especially because the particle diameters are so small, the viscous drag can be expressed, following Strauss [9], by use of Stokes Law. That is,

$$F_{drag} = 3\pi\mu DV_{rel} \tag{47}$$

where

μ = gas viscosity (lb-sec/ft^2)
D = particle diameter (ft)
V_{rel} = relative radial velocity (ft/s)

Since the radial relative velocity is

$$V_{rel} = -\frac{dr}{dt} \tag{48}$$

Newton's Second Law gives

$$m \frac{d^2r}{dt^2} - r\left(\frac{d\theta}{dt}\right)^2 = -3\pi\mu D \frac{dr}{dt} \tag{49}$$

where

m = particle mass (slugs)

Now, if we assume that the particles have a mass density equal to that of water (most particles are particulate laden water droplets in scrubber equipped stacks), then by using the following procedure we can determine how these particles would behave in the venturi:

$$m = \rho \frac{\pi D^3}{6} \tag{50}$$

where

ρ = mass density of water (slugs/ft^3)

Equation 44 can be put into nondimensional form by use of the following variables:

$$\left.\begin{aligned} \bar{r} &= r/R_o \\ \bar{t} &= tV_{\theta o}/R_o \end{aligned}\right\} \tag{51}$$

where $V_{\theta o}$ is the transverse velocity at the wall. The logic for the nondimensionalizing factor on time is that a time of $R_o/V_{\theta o}$ would be required for a particle to traverse R_o at constant speed $V_{\theta o}$. Other more logical typical times for the problem could be chosen, but we will conform to the practice previously established.

By use of these dimensionless variables Equation 49 becomes

$$\frac{d^2\bar{r}}{d\bar{t}^2} + \frac{1}{T}\frac{d\bar{r}}{d\bar{t}} - \frac{1}{\bar{r}^3} = 0 \tag{52}$$

where

$$T = \frac{D^2 \rho V_{\theta o}}{18 \mu R_o} \tag{53}$$

is a dimensionless constant.

Equation 52 has been solved by a fourth-order Runge-Kutta process to yield the dimensionless $\bar{r}$ as a function of time for the case of the cyclonic flow shown in Figure 41. For this case, the following values were used

$$\rho = 1.94 \text{ slugs/ft}^3$$

$$V_{\theta o} = 22.5 \text{ ft/sec}$$

$$\mu = 4.18 \times 10^{-7} \text{ lb sec/ft}^2$$

$$R_o = .5 \text{ ft}$$

The gas viscosity was chosen to be that for air at 100°C. Particle diameters, D, of 33, 50, 75 and 100 microns were used. An average axial velocity of 40 ft/sec results in a radial launch velocity of 6.69 ft/sec for a venturi angle of $\theta = 9.5^\circ$. This venturi angle is approximately that of the test venturi described in earlier.

Figure 44 shows particle trajectories for the cases above. The results show that, even for the largest particles, movement toward the center of the venturi throat is minimal and progress back toward the wall is rapid. The largest particle (100-micron diameter) reaches the wall in 0.014 s.

With an average axial velocity of 40 ft/s, this particle moves only 0.56 ft. down the venturi throat before being cast back to the wall. Recall that the particle is assumed to be convected axially with the gas flow. For the case considered by Peeler et. al. [10] to treat the particle's speed as a constant is not very accurate. However, in the case of cyclonic flow in a venturi throat, it is quite realistic, since the axial velocity is nearly constant across the throat.

This problem was also solved for the case of a launch angle of 45°, i.e., with the assumption that the 1-ft. diameter venturi throat section was being fed from a larger pipe with a very rapidly converging entrance section. Figure 45 shows particle trajectories plotted against the real time of flight for 100, 75 and 50 micron particles. Here, the particles have penetrated farther radially into the venturi throat, but they are flung to the wall almost as quickly as with the 9.5° launch angle. The mean axial convection velocity is 40 ft/s in both cases. Figure 46, which presents more data for the 45° launch situation, shows the trajectories for some very light particles (25 and 10 microns). These light particles are almost oblivious to the steep launch condition. They are seen to mostly amble (in a spiraling fashion) back toward the wall, taking longer to reach it.

Thus, it is apparent that the venturi will not, by itself, move the particles inward towards the center of the stack. In actuality, the intensification of the transverse velocity field by the venturi provides such a large radial acceleration field that the particles are moved back toward the wall in short times and axial distances. Based on the above results, Phase II efforts were concentrated on developing a low head loss flow straightener and evaluating its ability to redistribute the particulate. Further work on the venturi was discontinued.

5.2 WIND TUNNEL STUDIES ON FLOW STRAIGHTENERS

The device most frequently used to straighten cyclonic flow in ducts is an egg crate shaped grid which is baffled by a perforated cover plate on its upstream side [12-14]. Some handbooks and references prescribe a length of one pipe diameter for such a compound device [12]. The head loss across such an apparatus is so substantial that, in the case of stack applications, the flue gases and particulate would require additional boosting to be transported out of the stack. For this reason, a length of two pipe diameters was set as the initial test length for all the devices tested and the cover plate was omitted. Four configurations were tested: a D/6 egg crate straightener*, a D/4 egg crate straightener, a 4-vane étoile straightener, and an 8-vane étoile straightener. Typical devices are shown in Figures 47 and 48. The étoile devices were tested because of recent interest in the flow metering field in their effectiveness [15].

Wind tunnel tests were conducted on all these flow straightener devices. The same flow loop shown in Figure 5 was used for these tests. The swirl was induced by the tangential admittance device shown in Figure 9, and the straighteners were installed as shown in Figure 49.

The devices tested were constructed from 1/16-in. thick, 3003-H14 sheet aluminum because of its availability and workability. Initial test lengths of two pipe diameters were chosen, which allowed the devices to be shortened for further tests. Each device was located, as shown in Figure 49, 10 pipe diameters downstream from the swirl generator to allow the flow pattern to stabilize before entering the straightener. Enough room was left downstream from the straightener to allow a sampling station to be located 10 ft. further downstream to be used to obtain velocity profile data for the straightened flow.

---

* A D/6 egg-crate has a cell size 1/6 the stack diameter, D.

Each straightening device was tested at flow rates of 20, 30 and 40 cubic ft^3/s. Head loss data for each device were obtained at swirl generator settings of 7, 18, 20, 22 and 24 in. for each flow rate. These settings of the vane control rod produced increasing swirl intensities in the cyclonic flow. Table 3 shows the swirl characteristics for each of the settings. These data were calculated from accumulated velocity field data measured with the three-dimensional probe. Downstream velocity profile data were taken only at a maximum swirl generator setting. Readings were taken at each 1-in. interval of the pipe's diameter for the velocity field. If the device sufficiently straightened the flow (outlet $m \leq 0.1$), the device was then shortened and retested. This process continued until the device failed to straighten the flow.

5.3 RESULTS OF WIND TUNNEL STUDIES

Figures 50, 51 and 52 show head loss as a function of swirl intensity and straightener length for a D/6 straighteners at 3 different flow rates (20, 30 and 40 ft^3/s). These flow rates are equivalent to average axial velocities of 11.3, 17.0 and 22.6 ft/s, respectively. The corresponding Reynolds numbers are in the 10^5 range.

These results indicate that head loss increases as swirl intensity increases and, as expected, that head loss increases as flow rate increases. Also evident is a decrease in head loss as straightener length decreases, but only to a certain point. Head loss in the presence of cyclonic flow appears to reach a relative minimum, with straightener length equal to the cell size. This minimum point represents the smallest amount of energy required to straighten a swirling flow.

Typical effects of the honeycomb straightening device on the approaching cyclonic velocity fields are shown in Figures 53 and 54. In these figures, the approach flow is shown by the solid line with the square data points; the downstream, or "straightened" flow, is shown by the line with circular data points. It is apparent that the axial component of the swirl flow field has been altered from a classical cyclonic profile to a nearly rectangular profile in passing through the straightening device, and the strong swirl component in the approach flow has been eliminated by the straightening vanes.

For the straightener with a cell size of D/4, comparable results were obtained. Figure 55 shows typical head loss data for the maximum flow rate tested. This straightener did not effectively remove the swirl components of the velocity field for a length shorter than the cell size, D/4. Figures 56 and 57 show how effectively a D/4 egg crate straightens swirling flow.

Results of the head loss studies on the étoile devices are shown in Figures 58 and 59 for 4 and 8-vane straighteners, respectively. It was found that a length of two pipe diameters is the minimum effective length for the 8-vane étoile straightener. Yaw angles of 15^{o} were encountered when the length was reduced. Surprisingly, the 4-vane étoile straightener is effective at a length of one pipe diameter. Yaw angles of 24^{o} were observed when the overall length was reduced to 1/2 pipe diameter. Figures 60 and 61 demonstrate how effectively a 4-vane étoile device of length D straightens flow.

Overall, the wind tunnel data show that the egg crate device is superior to the étoile device based on head loss considerations. In addition, the data show that in cases where cyclonic flow is not used as a control device, it can be economically advantageous to straighten the flow. For example, for sufficiently tall stacks with swirling flows of common intensity, the total head loss from the straightening device to the stack exit can be less for the straightened flow than for the case where no straightener is used, as shown by the following procedure:

In Reference 2, the following empirical relation is given for head loss in a round pipe with swirling flow.

$$\Delta P_{swirl} = \rho V_z^2 \frac{L}{D} [0.8f(1 + \bar{m})^2 - 1.43 \times 10^{-3}] \quad (54)$$

where

$$f = f_o(1 + .196\ m_1^3 - .41\ m_1^2 + .344\ m_1) \quad (55)$$

and

$$\ln m_2/m_1 = -1.1\ f\ L/D \quad (56)$$

with

F = friction factor for swirling flow,
f_o = friction factor for straight flow,
m_1 = flue stack inlet swirl intensity,
m_2 = flue stack outlet swirl intensity,
L = length of stack (ft),
D = diameter of stack (ft),
ρ = fluid mass density (slugs/ft^3),
$\bar{m}$ = $(m_1 + m_2)/2$,
$\bar{V}_z$ = average axial velocity (ft/s).

The combined head loss due to the straightening device and straightened flow through the balance of the stack is

$$\Delta P_{st} = \Delta P_{device} + f_o \frac{L}{D} \bar{V}_z^2 \qquad (57)$$

where the symbols have the same meaning as in Equations 54-56.

As an example, consider a galvanized steel stack of variable length with a diameter of 18 in. Calculations for three flow rates (20, 30 and 40 ft^3/s) show that the V_z values are 11.32, 16.98 and 22.64 ft/s, respectively. The roughness ratio e/D is 0.00033 and the respective Reynolds numbers are 9.3×10^4, 1.4×10^5, and 1.85×10^5 if we assume air at ambient temperature. From a Moody diagram, the friction factors (f_o) are 0.020, 0.0182, and 0.0178, respectively. Equation 55 is used to find the equivalent swirl friction factor and Equation 56 is used to determine m_2. The inlet swirl intensities for the three flow rates are taken to be m_1 = 0.859, 0.808, and 0.797, respectively. These values are compatible with a particular swirl generator setting used in our laboratory and representative of actual conditions encountered in stacks.

The results from these calculations are shown in Figure 62. The dashed lines indicate head losses associated with the cyclonic flows and the solid lines indicate the head losses required to straighten the flow with a straightener of length D/4 and to push the straightened flow out the stack. The cross-hatched area in Figure 62 shows that for sufficiently tall stacks it is more economical to straighten the flow than to not straighten it.

The results shown in Figure 62 are for the flow of air at 70°F. For higher temperature air the friction factor, f_o, used in equations 54 through 57, would change according to a standard Moody diagram where the dependence is through the Reynolds number. If the flow rates are high enough to be in the "fully rough zone" the friction factor, f_o, is a function of the wall roughness only. If the flow rate yields a Reynolds number in the "transition zone" then increasing the temperature of the air will lower the Reynolds number and, hence, increase the friction factor, f_o. This will cause both the dashed and solid line head loss curves of Figure 62 to have increased slopes. Consequently, the bounding curve of the cross-hatched region will shift to the left. However, the general shape of the cross-hatched region will remain the same. No data is available on the head losses across egg crate straightners at elevated temperatures. A reasonable expectation is that the losses would increase proportional to the increase in the friction factor, f_o.

5.4 FIELD EVALUATION OF EGG CRATE ASSEMBLY

The ability of the egg crate to straighten cyclonic flow and to redistribute particulate was evaluated at a fertilizer plant after the wind tunnel studies were completed. The stack was 30 in. in diameter and 45 ft. high. Stack temperature was 90°F, moisture was 5%, and the axial volumetric flow was approximately 4500 ft^3/min. Exhaust gases from the fertilizer blending operation entered tangentially at the base of the stack, and then passed through a water spray chamber and a turning vane to produce swirling flow. The swirling flow caused particulate laden water droplets to move to the stack wall where they drained downward and exited with the scrubber water.

A galvanized steel egg crate with cell size D/4 (7.5 in.) and length D/2 (15 in.) was installed in the stack at a point seven diameters (18 ft.) downstream of the turning vane (4 diameters from the stack exit). Particulate and velocity measurements were made through sampling ports located two pipe diameters downstream and two pipe diameters upstream from the center of the egg crate. EPA Reference Methods 1 (sampling point selection), 2 (velocity and volumetric flow), and 5 (particulate sampling) were used in the testing.

Flow angle with respect to the stack longitudinal axis was measured using a United Sensor ® three-dimensional pitot tube. Velocity measurements upstream of the egg crate (Table 4) confirmed that a strong swirling flow (swirl intensity factor, m = 0.65) was present in the stack, e.g., flow angles up to 70° were measured near the center of the stack. In contrast, flow angle measurements at corresponding points downstream of the egg crate never exceeded 4° - well within the EPA definition of noncyclonic flow. Further, static pressure measurements upstream and downstream of the egg crate were identical, demonstrating that the head loss was negligible. Thus, we conclude that the egg crate can be a cost-effective means to destroy cyclonic flow patterns.

The tests to determine the effect of the egg crate on the particulate distribution were inconclusive. In these tests, eight 60-minute sampling runs were accomplished using two Method 5 trains sampling simultaneously. (Train A sampled two pipe diameters downstream of the egg crate and Train B sampled two pipe diameters upstream.) In the first three runs, each train sampled a total of 20 points (10 points on each diameter). In these and the other five runs, Train A sampled with its nozzle and pitot tube aligned with the stack axis while Train B sampled with its nozzle and pitot tube aligned with the direction of the gas flow at the sampling point. Also, Train B's sampling time at each point was adjusted using Equation 58 so that the ratio of the volume of gas collected at each point to the total axial volumetric flow in the stack remained constant.

where:

t_1 = nominal sampling time per point (60 min/20 sampling points),
t_2 = actual sampling time per point,
θ^2 = angle between flow direction and stack axis.

In the last five runs, single-point sampling rather than traversing was employed. In these runs, Train A sampled at the same point - a point 23 in. in from the port hole, but Train B sampled a different point in each run, i.e., Run 4 (28 in.), Run 5 (26.5 in.), Run 6 (24.7 in.), Run 7 (23 in.), and Run 8 (19.3 in.). The objective of these five runs was to determine the particulate distribution upstream of the egg crate in relation to the concentration at a specific point downstream of the egg crate.

The results of the eight runs (Table 5) show that in all runs the particulate concentration determined upstream compared well with that determined downstream. Further, the close agreement between the two trains in the last five runs (where single-point sampling was employed) shows that the particulate concentration was evenly distributed upstream of the egg crate. This demonstrates that the swirling flow effectively removed large particles, i.e., the remaining particles were small enough to act like a gas. Thus, the degree of redistribution of particulate by the egg crate cannot be determined from these results.

Resource limitations and the fact that no additional sources were available for testing prevented conducting additional field tests.

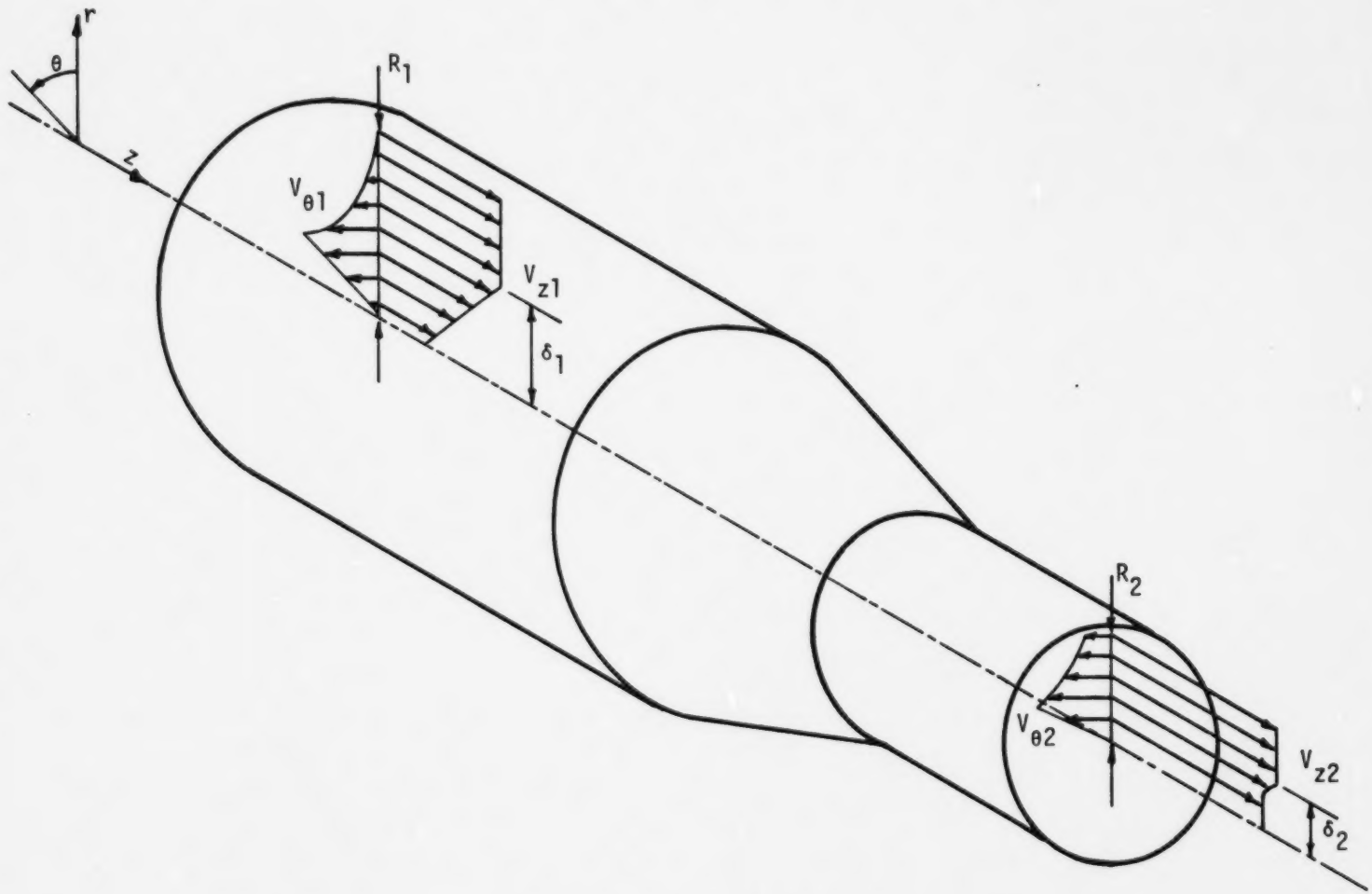

Figure 1. Definition sketch.

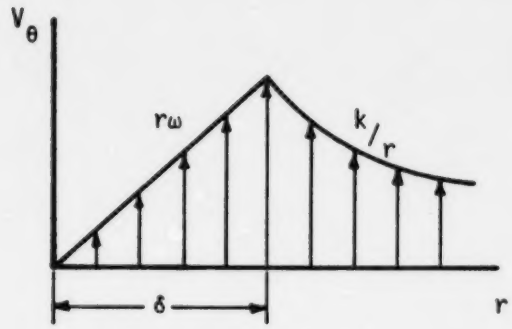

Figure 2. Variation of transverse velocity.

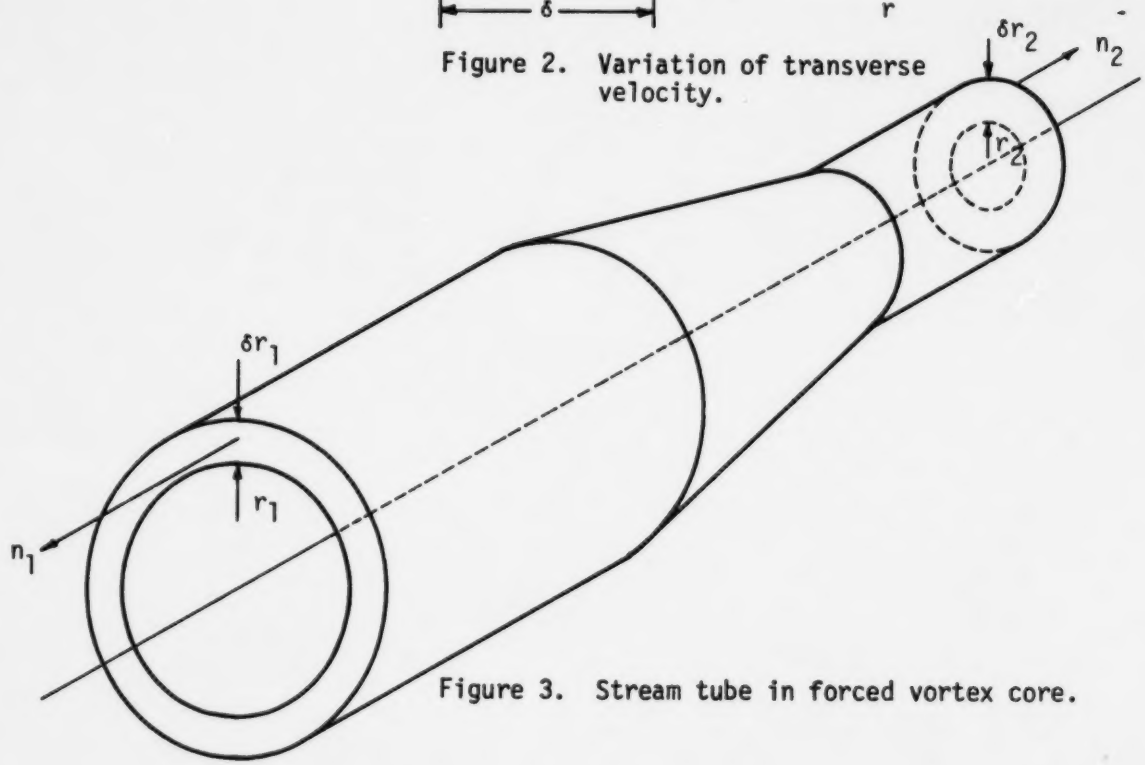

Figure 3. Stream tube in forced vortex core.

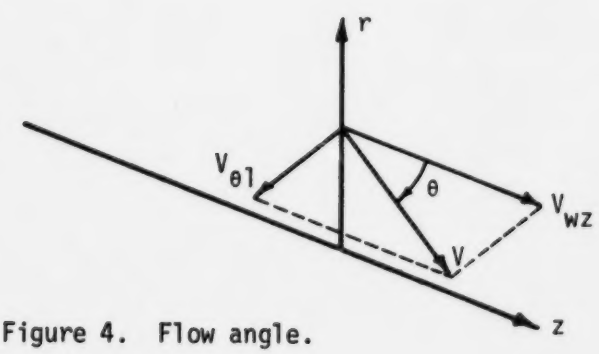

Figure 4. Flow angle.

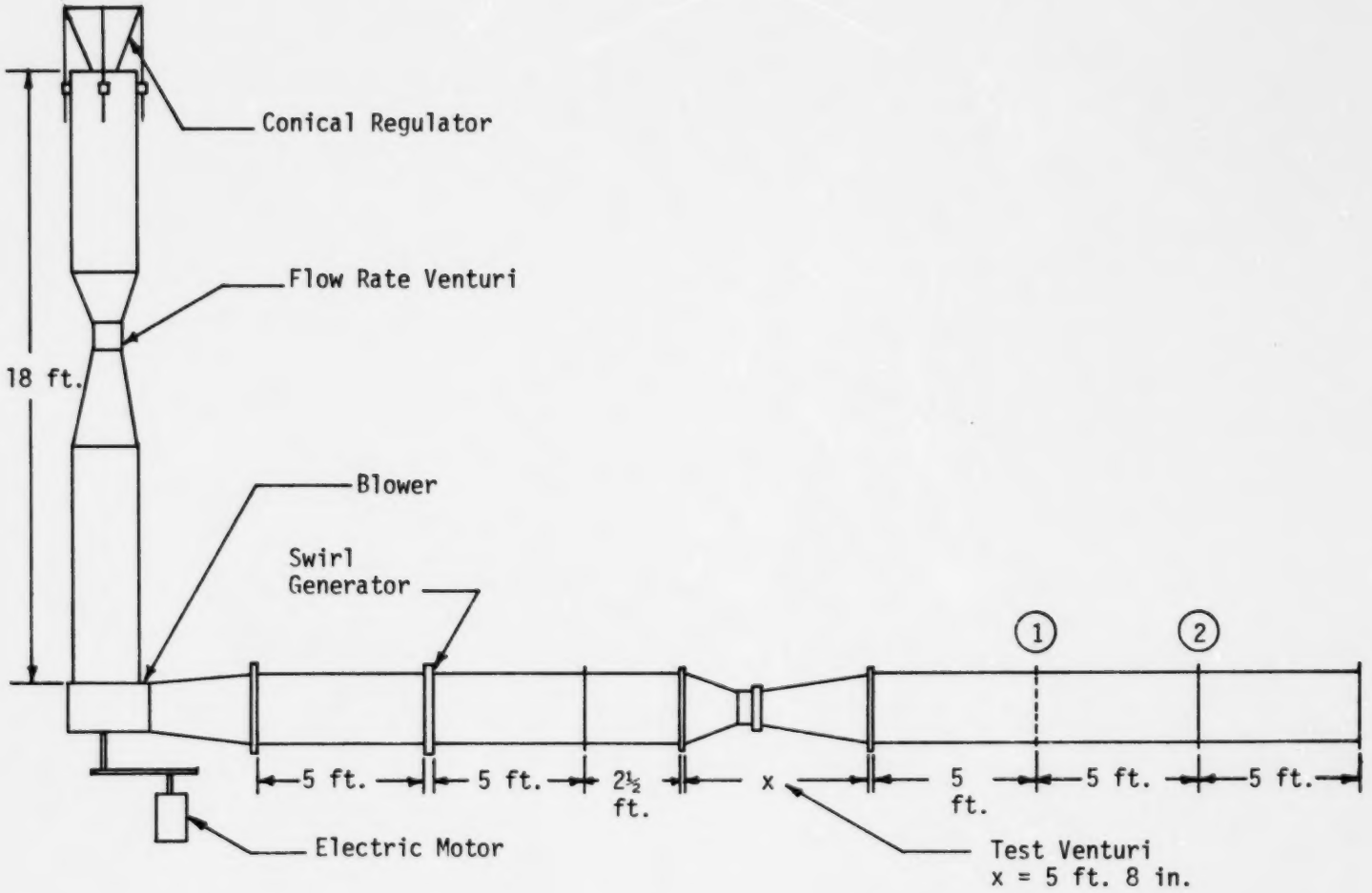

Figure 5. Schematic of experimental facility.

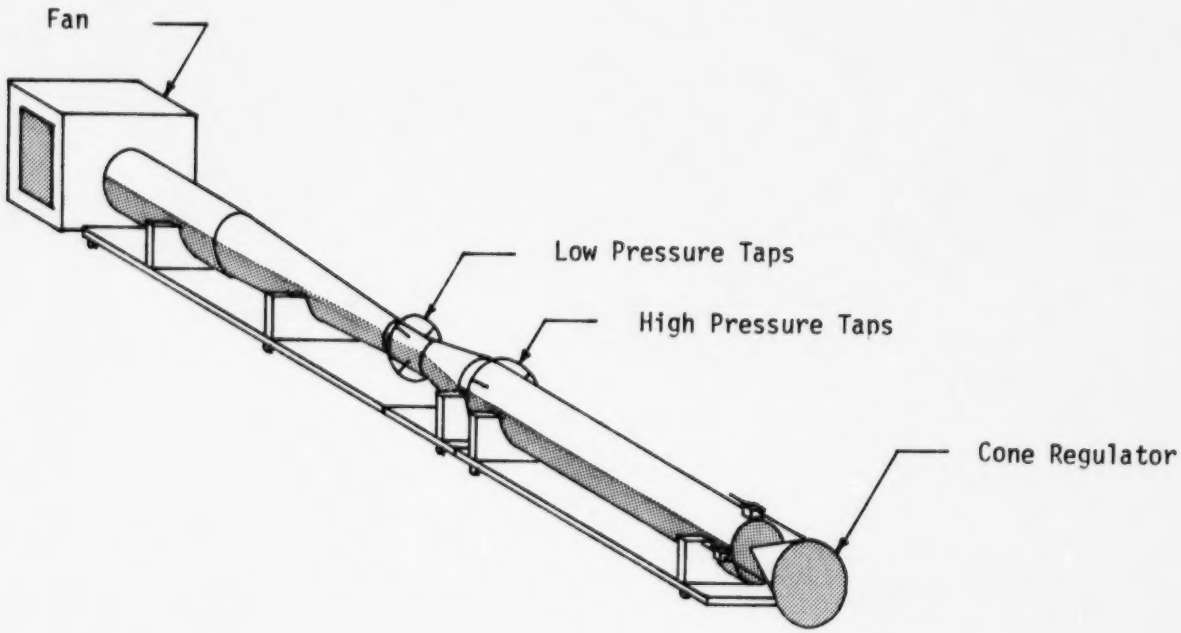

Figure 6. Flow measurement and regulation.

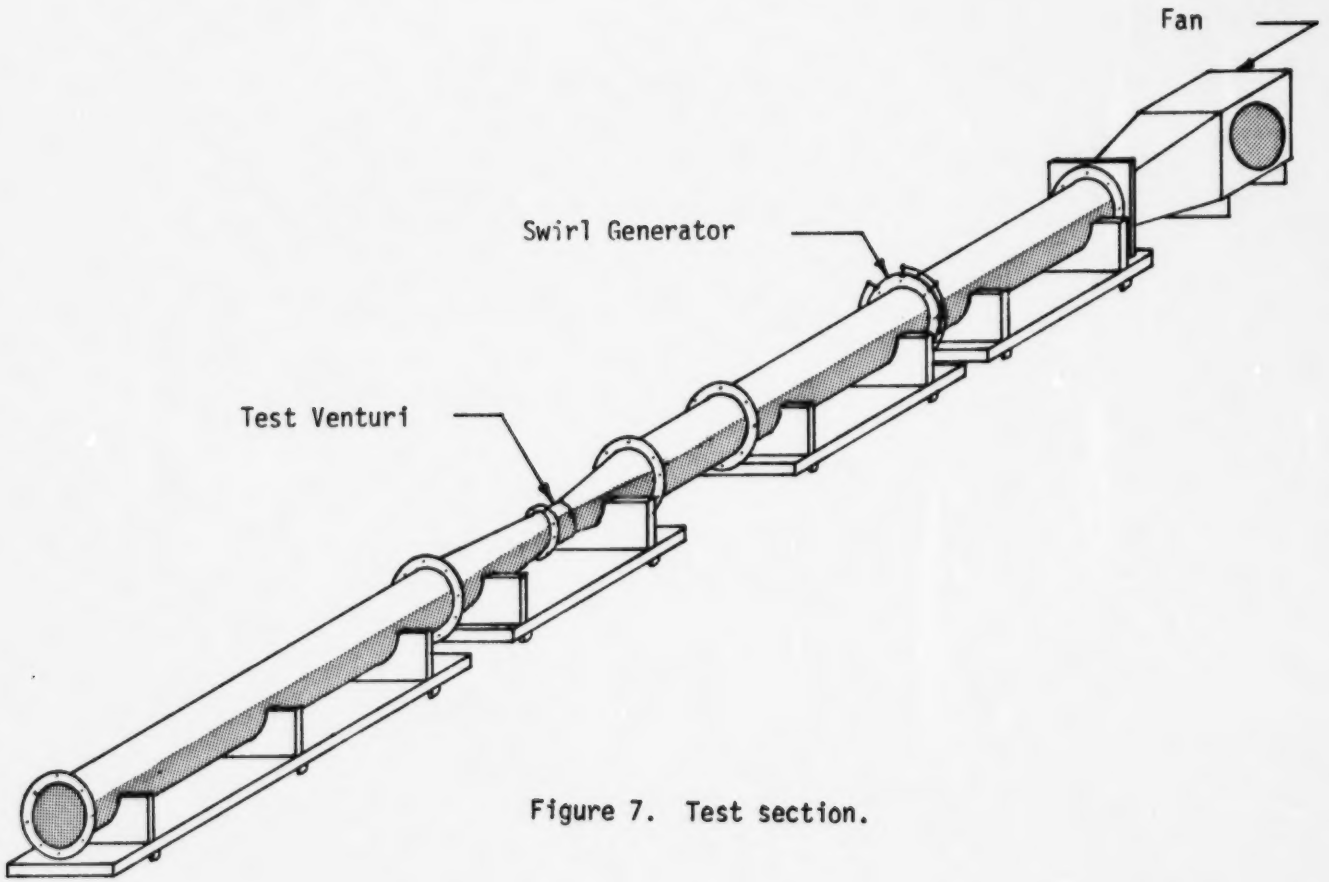

Figure 7. Test section.

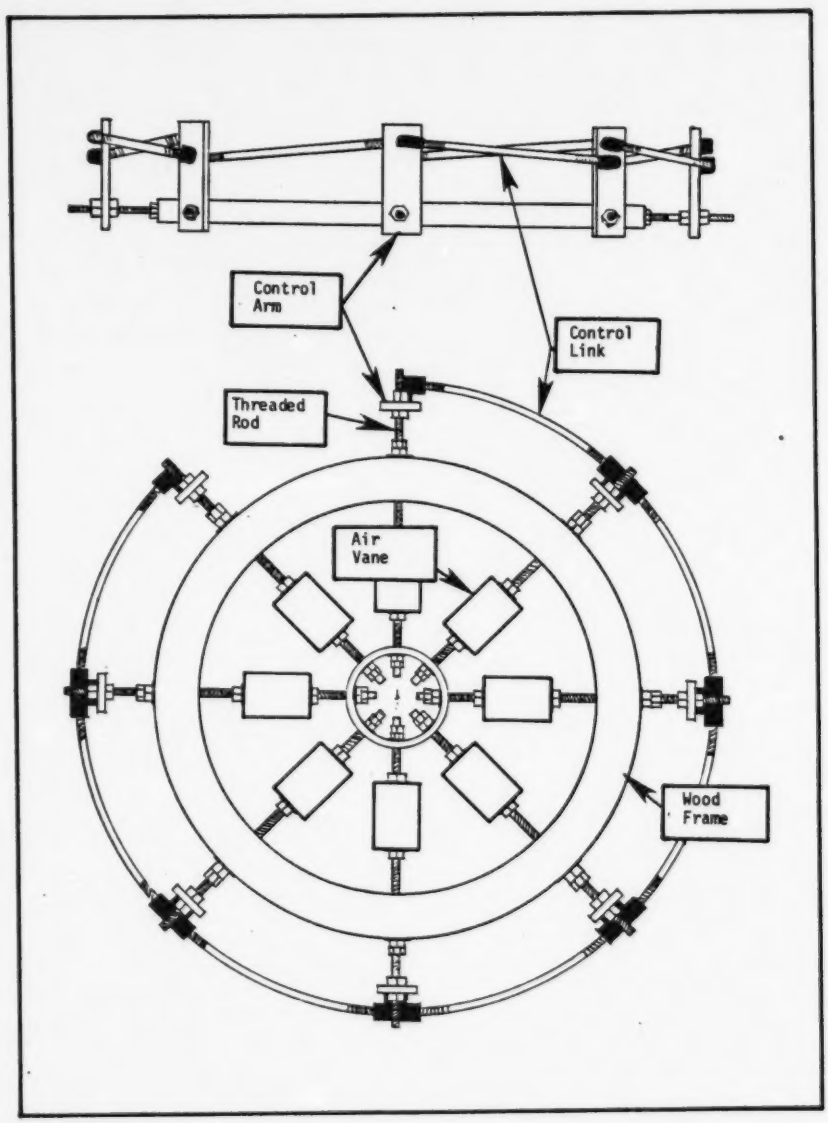

Figure 8. Vane-type swirl generator.

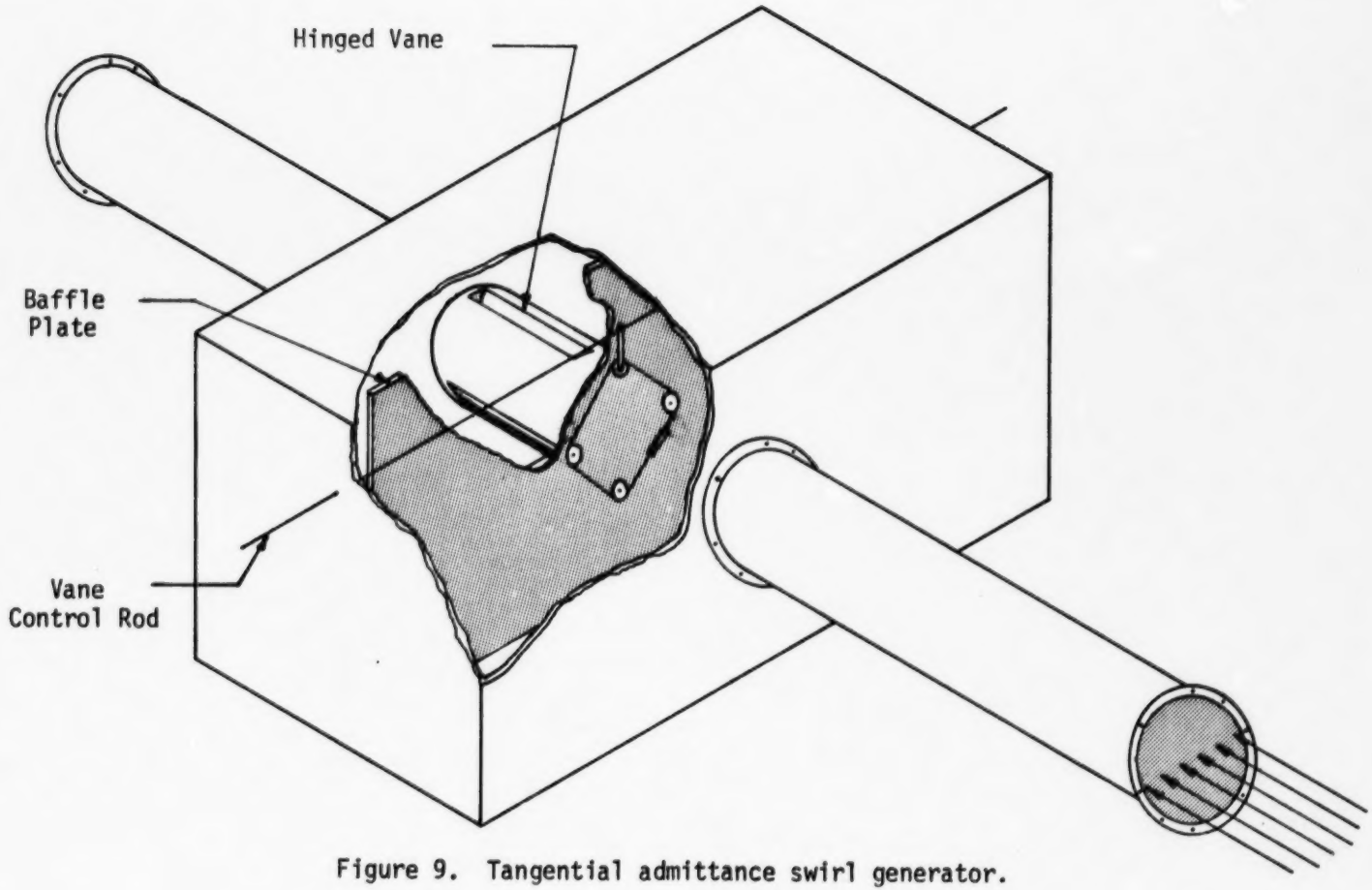

Figure 9. Tangential admittance swirl generator.

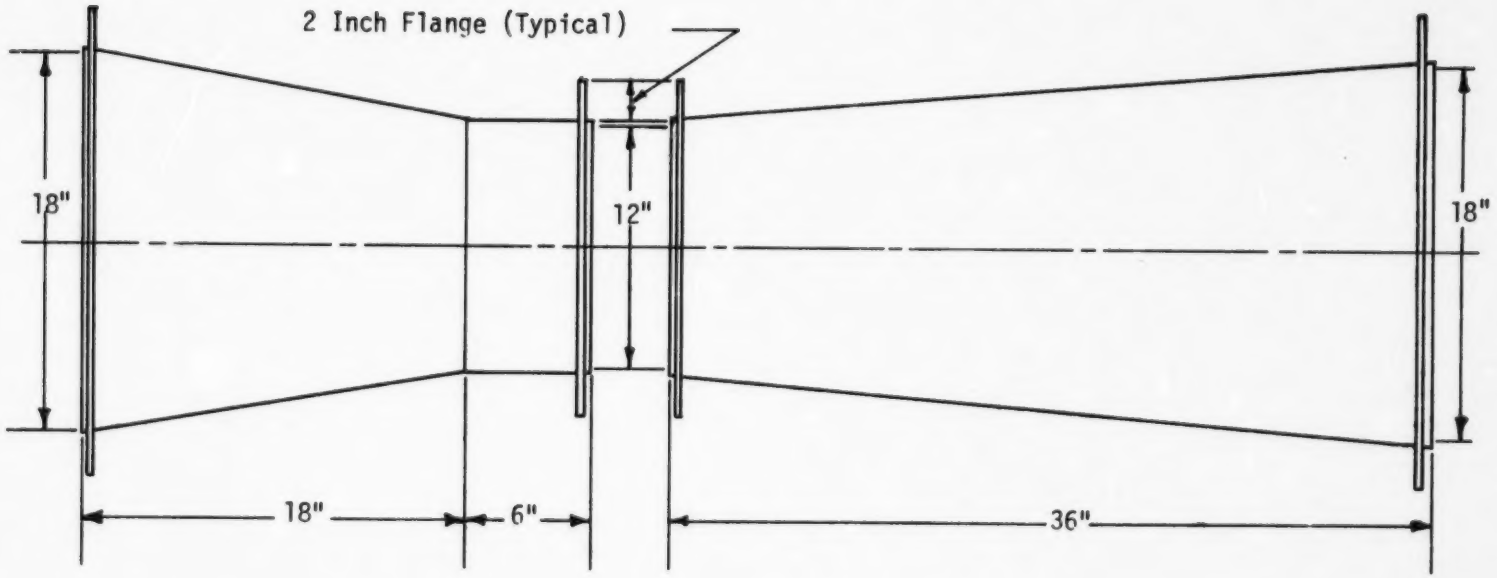

Figure 10. Test venturi.

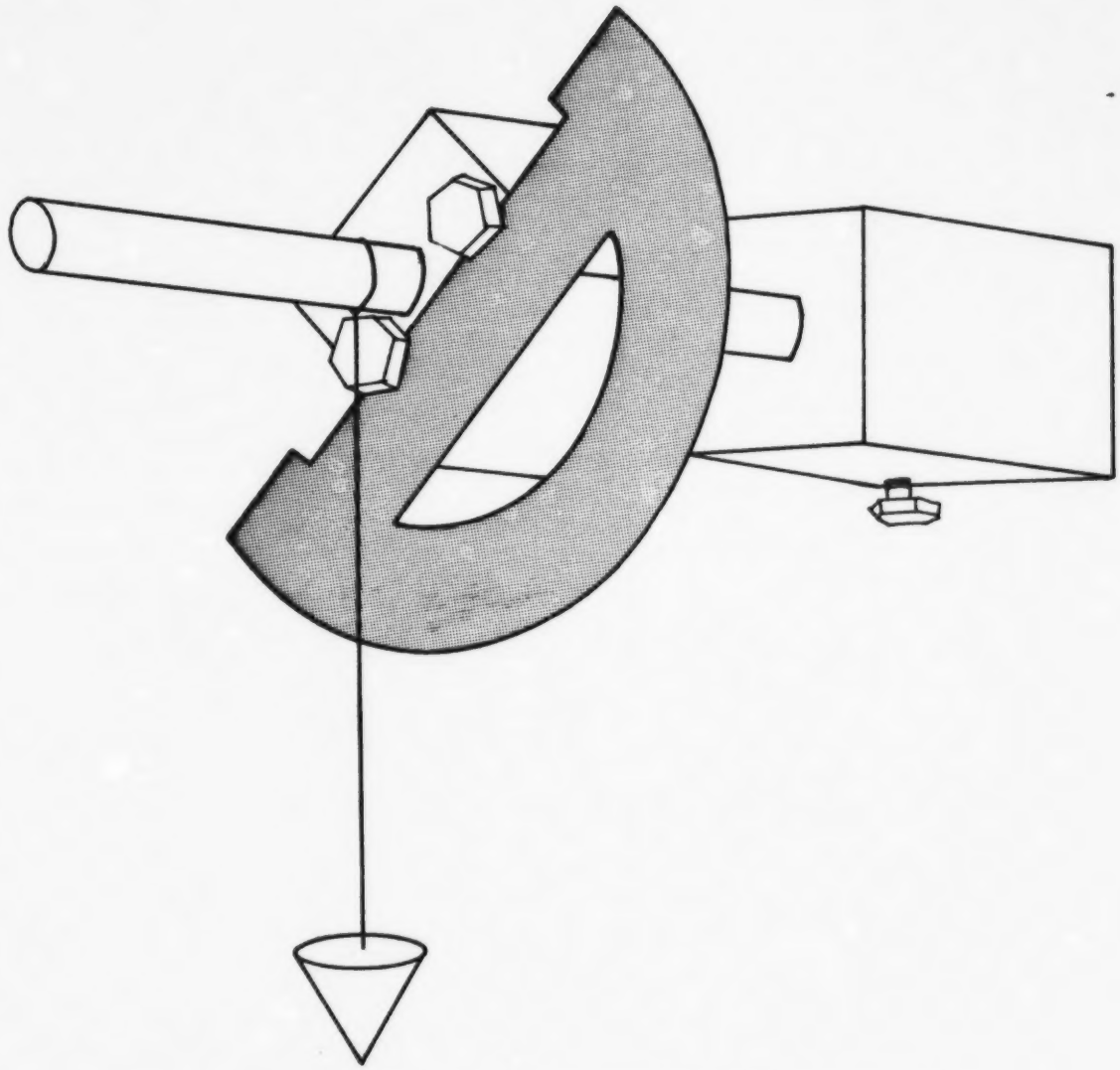

Figure 11. Protractor-sampling block assembly.

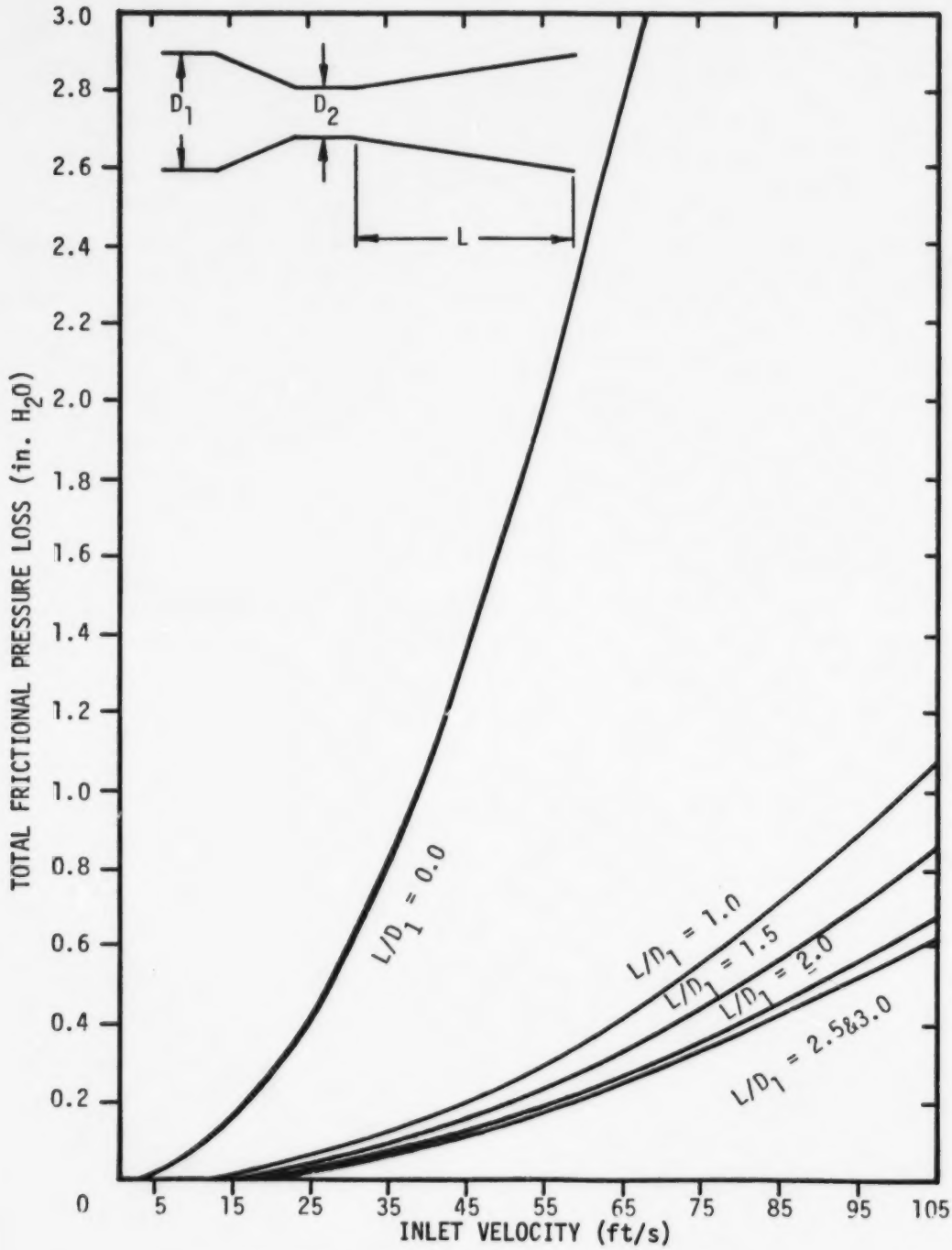

Figure 12. Frictional losses across a venturi.

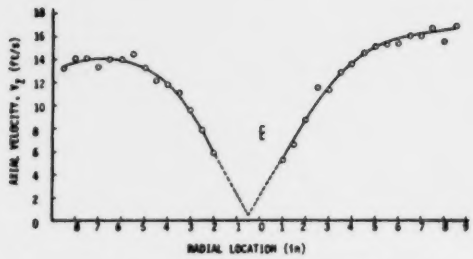

Figure 13. Axial velocity component at venturi entrance.

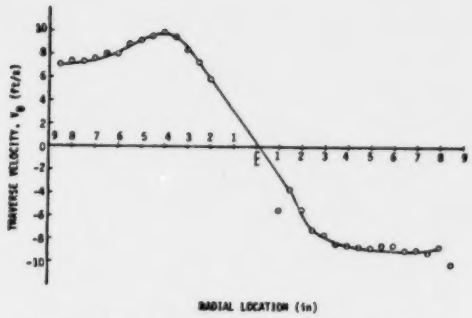

Figure 14. Traverse velocity component at venturi entrance.

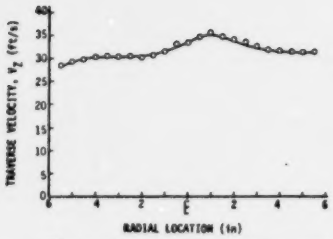

Figure 15. Axial velocity component at venturi throat.

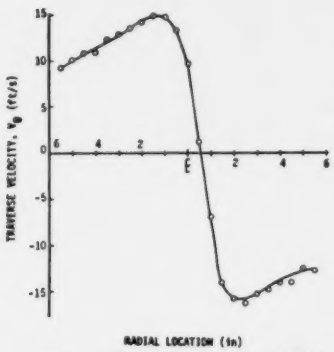

Figure 16. Transverse velocity component at venturi throat.

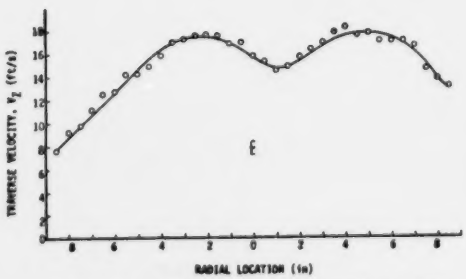

Figure 17. Axial velocity component at venturi exit.

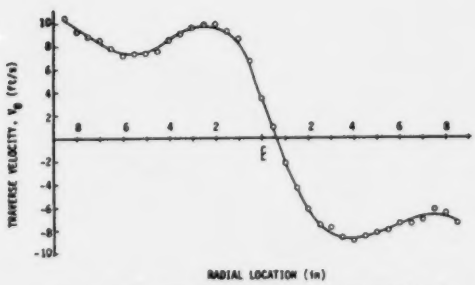

Figure 18. Transverse velocity component at venturi exit.

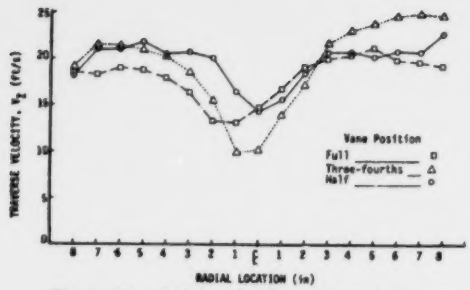

Figure 19. Axial velocity component at venturi entrance.

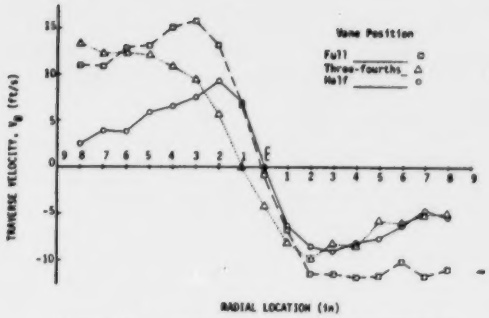

Figure 20. Transverse velocity component at venturi entrance.

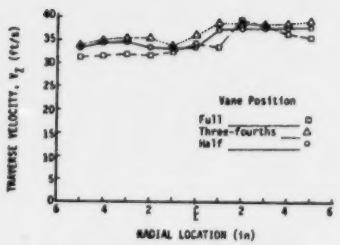

Figure 21. Axial velocity component at venturi throat.

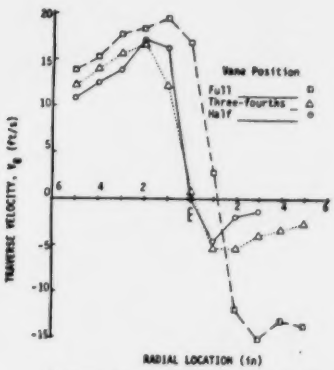

Figure 22. Transverse velocity component at venturi throat.

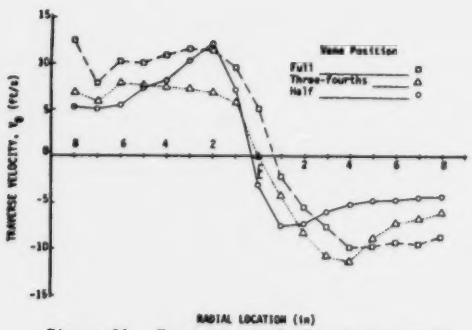

Figure 24. Transverse velocity component at venturi exit.

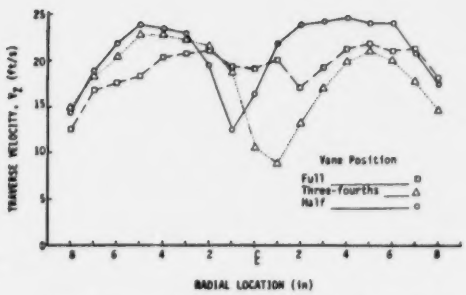

Figure 23. Axial velocity component at venturi exit.

Figure 25. Axial velocity component 5 ft downstream from venturi exit.

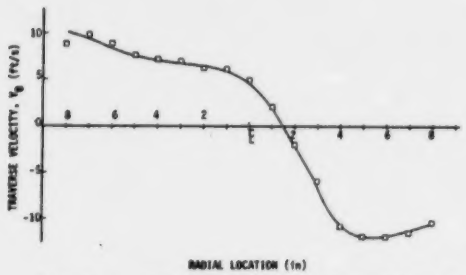

Figure 26. Transverse velocity component 5 ft downstream from venturi exit.

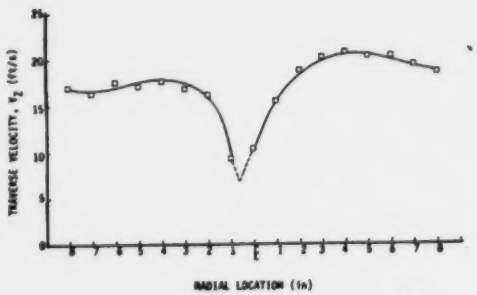

Figure 27. Axial velocity component 10 ft downstream from venturi exit.

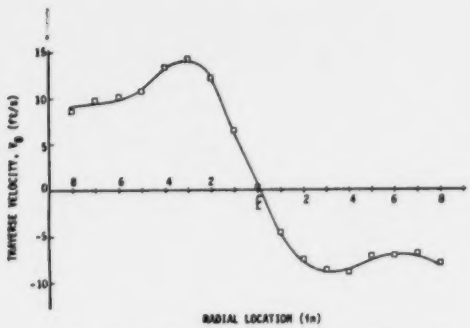

Figure 28. Transverse velocity component 10 ft downstream from venturi exit.

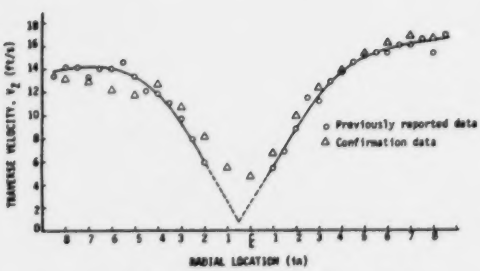

Figure 29. Axial velocity component at venturi entrance.

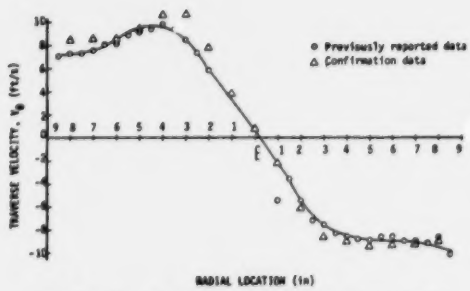

Figure 30. Transverse velocity component at venturi entrance.

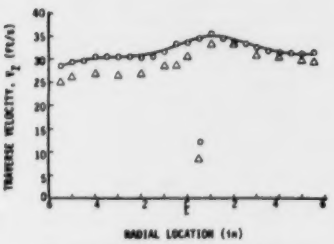

Figure 31. Axial velocity component at venturi throat.

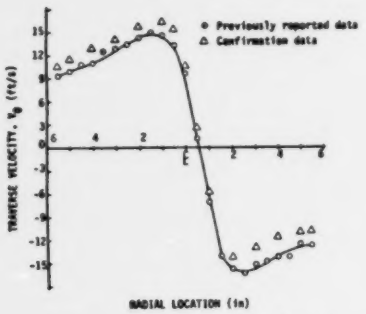

Figure 32. Transverse velocity component at venturi throat.

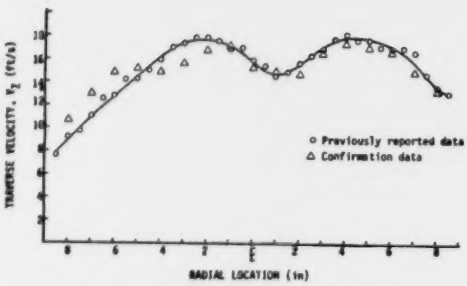

Figure 33. Axial velocity component at venturi exit.

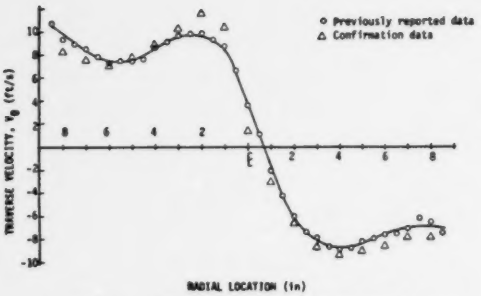

Figure 34. Transverse veolcity component at venturi exit.

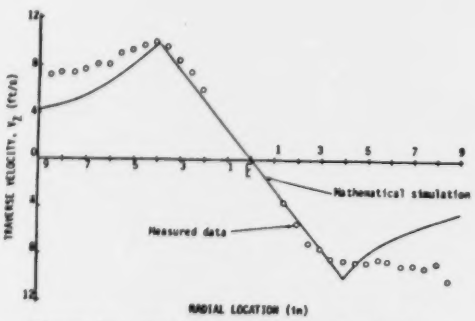

Figure 35. Transverse velocity, V_θ simulation (approaching the venturi).

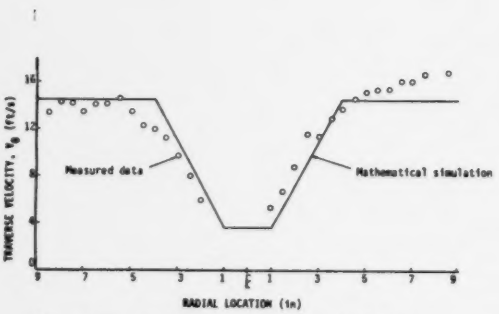

Figure 36. Axial velocity, V_z, simulation (approaching the venturi).

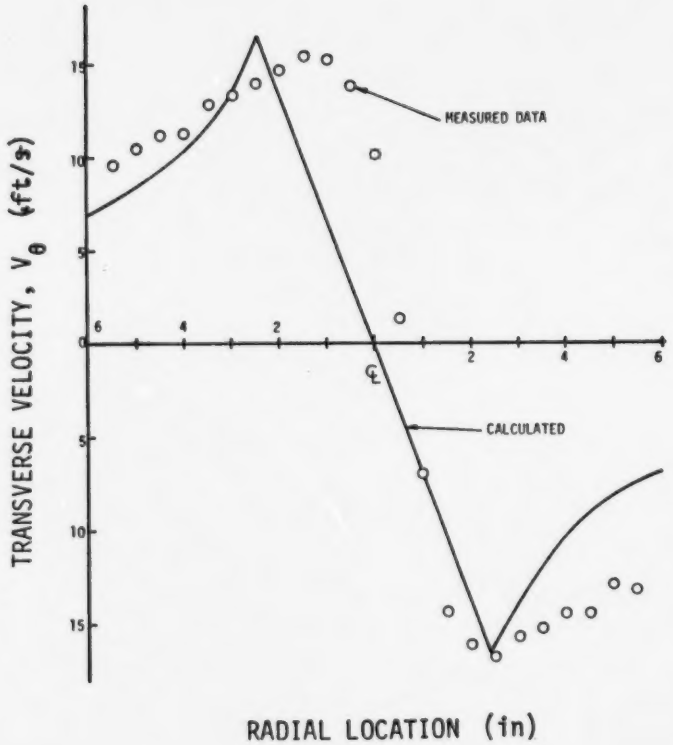

Figure 37 Transverse velocity, V_θ, (calculated at throat).

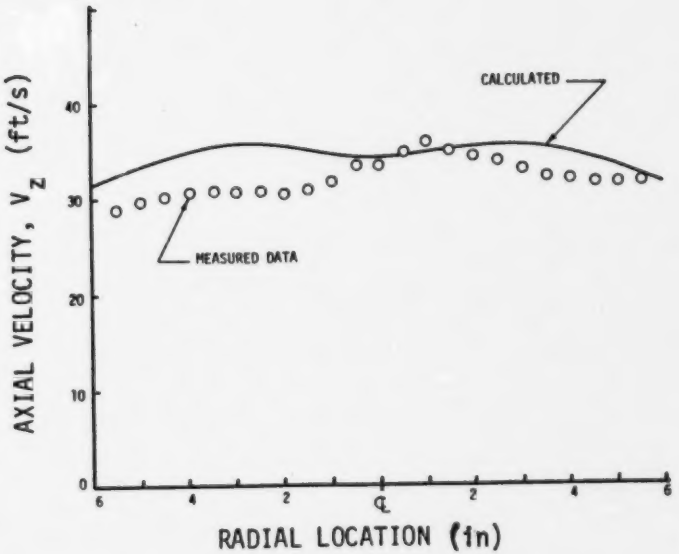

Figure 38 Axial velocity, V_z (calculated at throat).

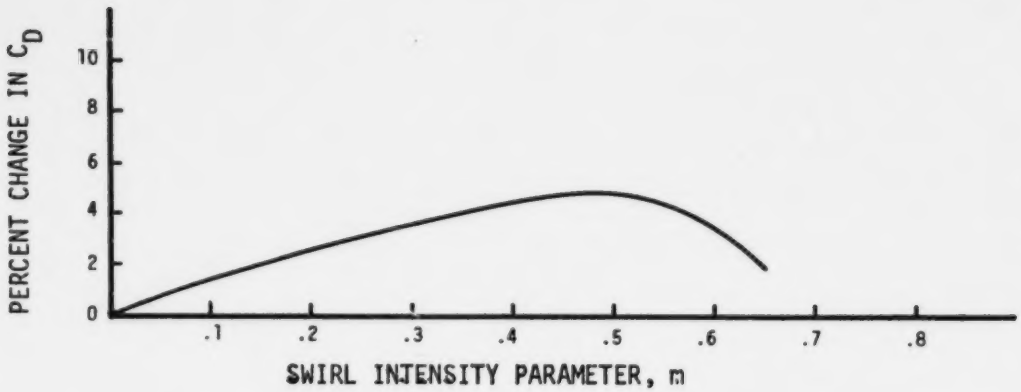

Figure 39. Percent change in discharge coefficient for orifice plate [7].

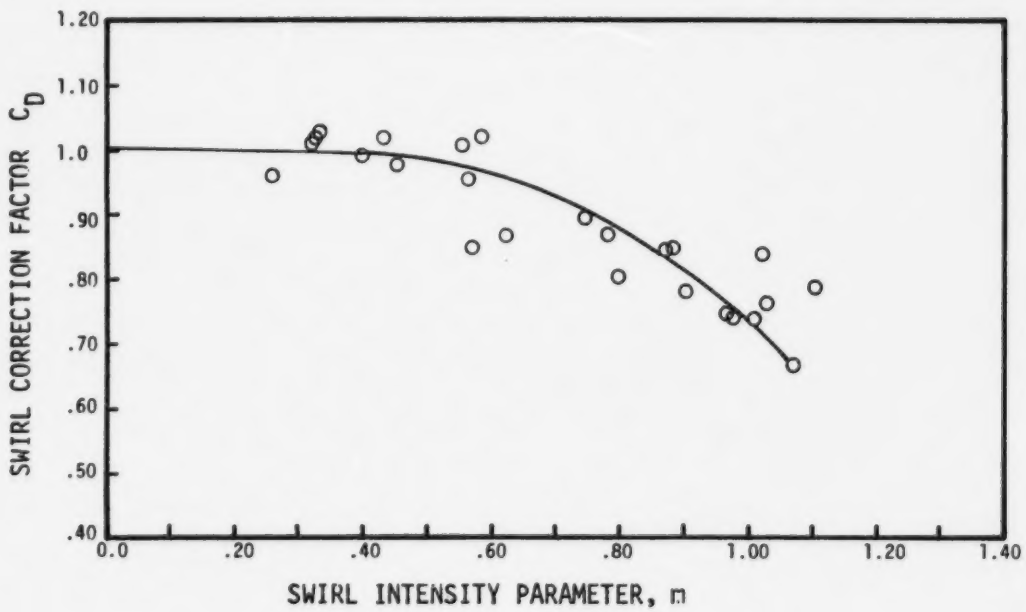

Figure 40. Swirl correction factor "C_D" vs. swirl intensity "m"

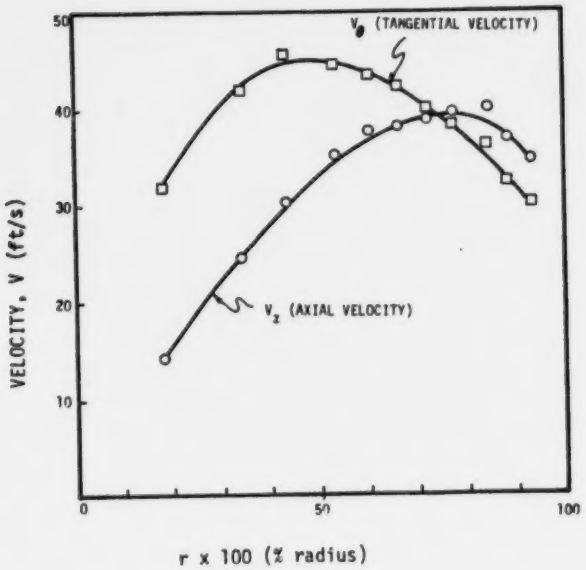

Figure 41. Axial and tangential fluid velocities along stack radius for cyclonic flow [10].

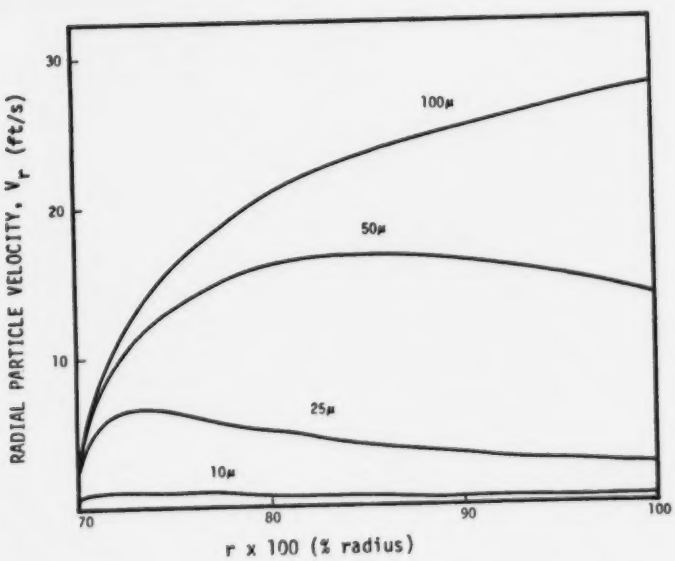

Figure 42. Radial particle velocities in cyclonic flow for particles starting at 70% of stack radius [10].

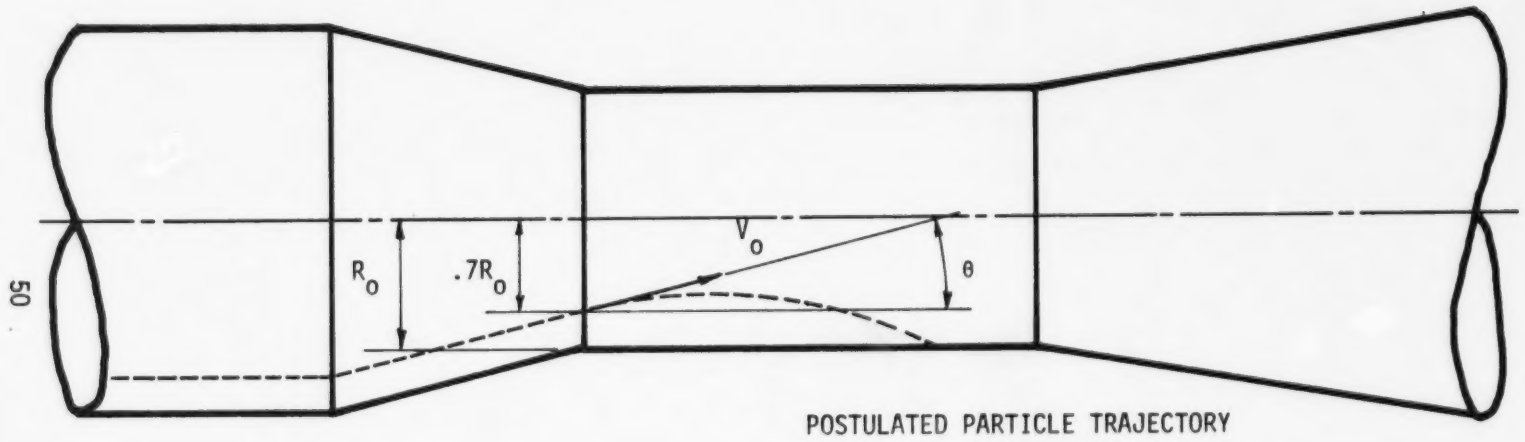

Figure 43. Particle launch conditions in venturi throat (dashed line shows postulated trajectory).

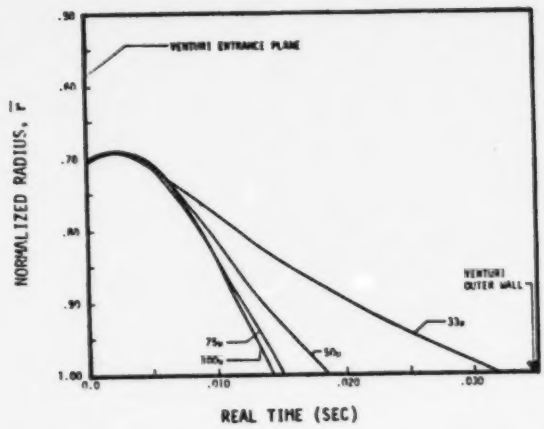

Figure 44 Particle trajectories in venturi throat for 9.5° launch angle.

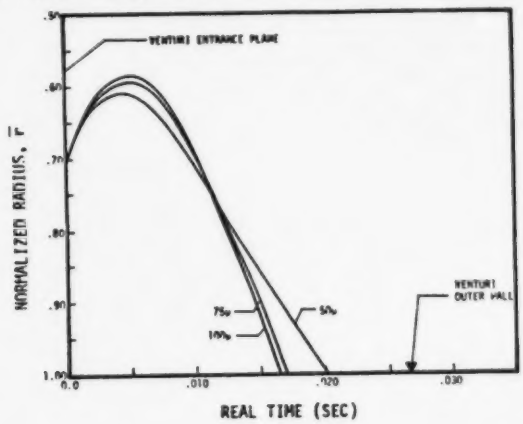

Figure 45 Particle trajectories in venturi throat for 45° launch angle.

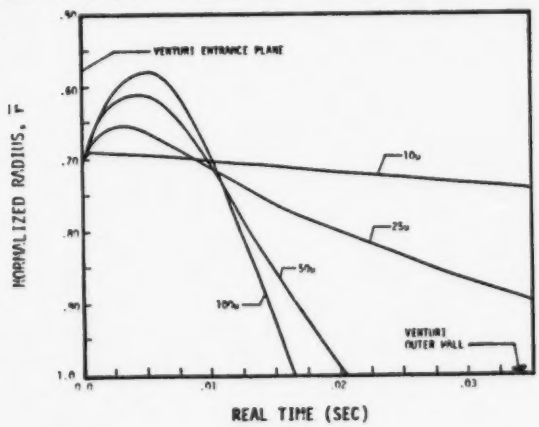

Figure 46 Particle trajectories in venturi throat for 45° launch angle.

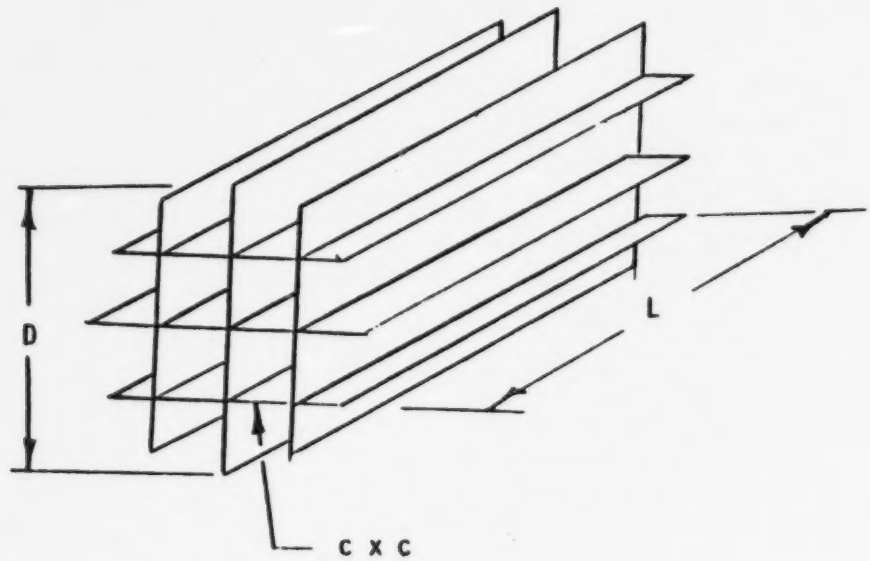

Figure 47. D/4 egg crate flow straightener.

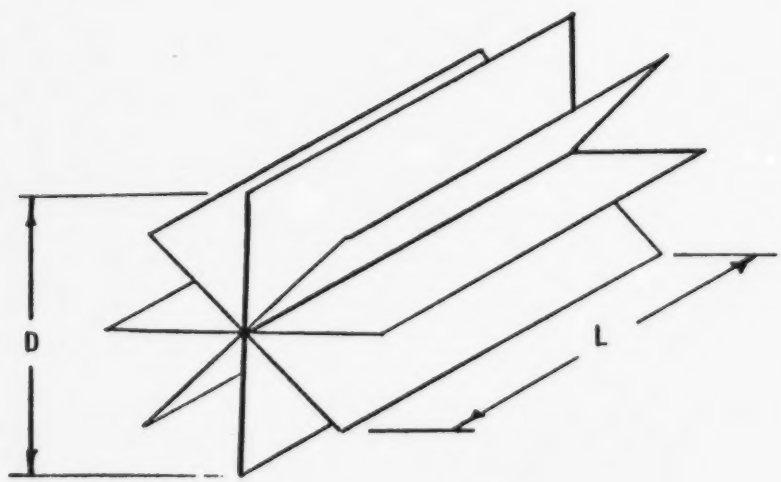

Figure 48. Eight-vane etoile flow straightener.

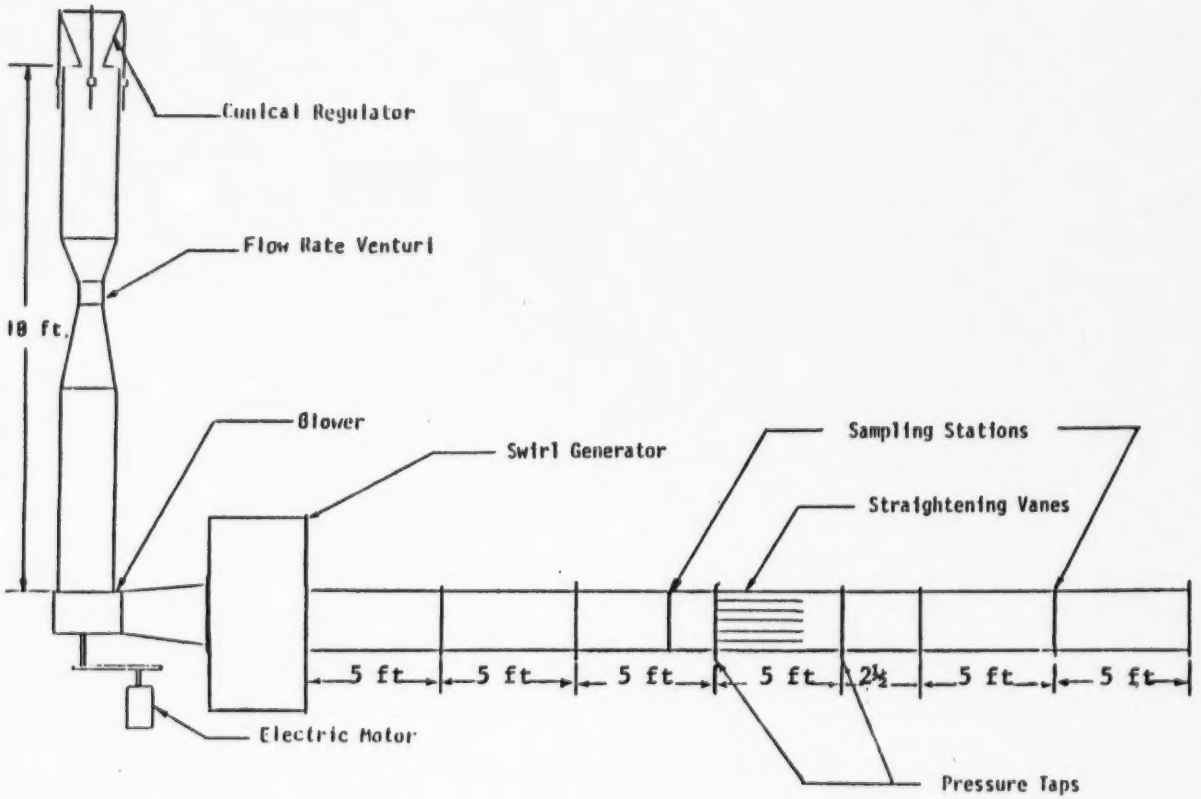

Figure 49. Schematic of experimental facility for straightener tests.

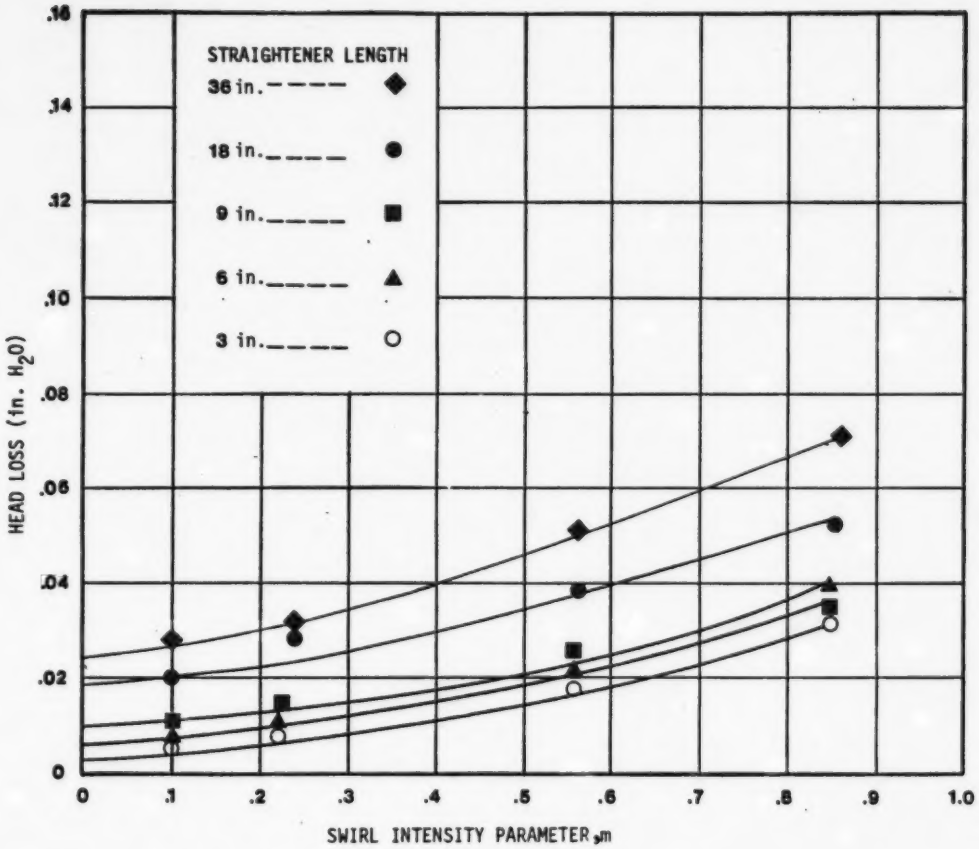

Figure 50. Head loss vs. swirl intensity for a D/6 egg crate flow straightener (flow rate = 20 ft^3/s).

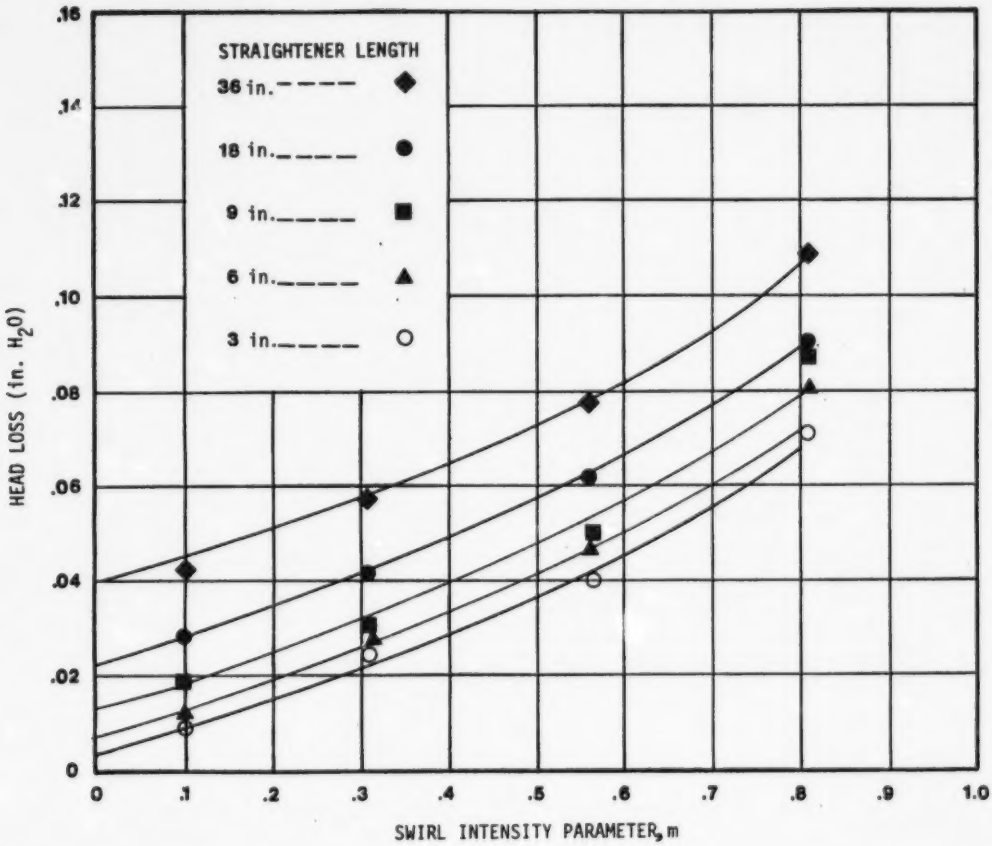

Figure 51. Head loss vs. swirl intensity for a D/6 egg crate flow straightener (flow rate = 30 ft^3/s).

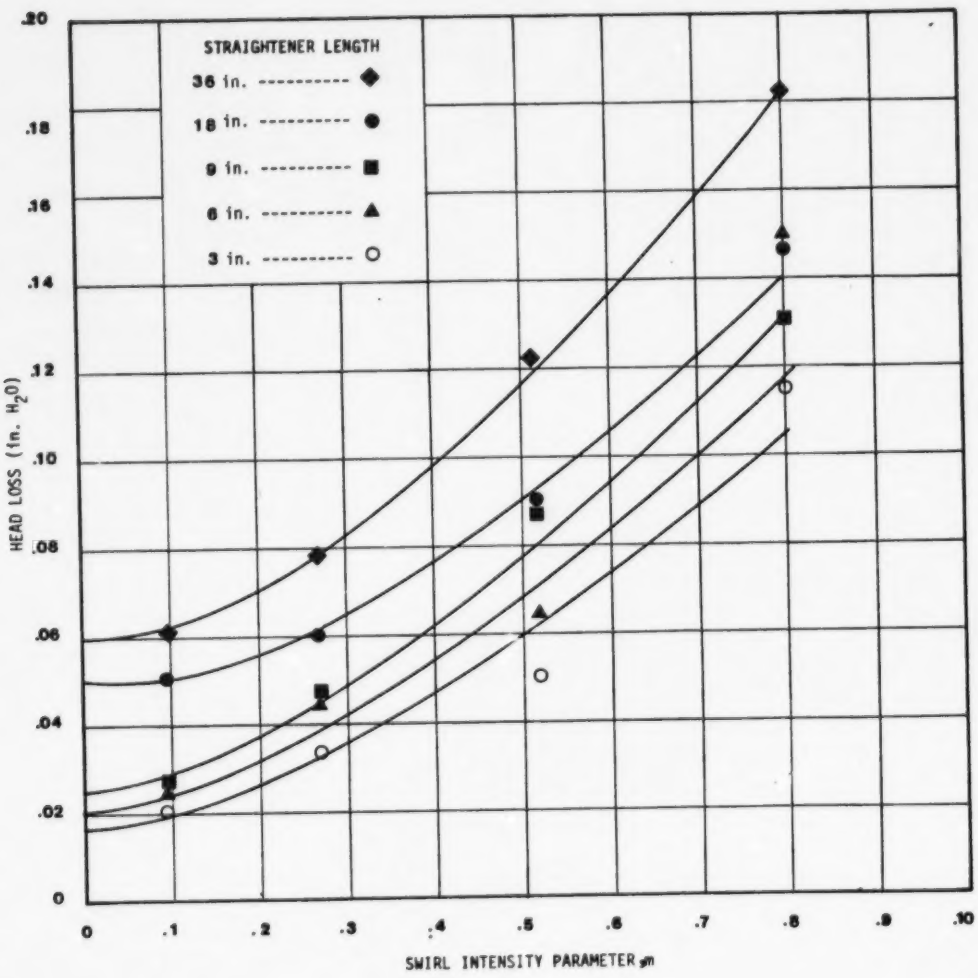

Figure 52. Head loss vs. swirl intensity for a D/6 egg crate flow straightener (flow rate = 40 ft^3/s).

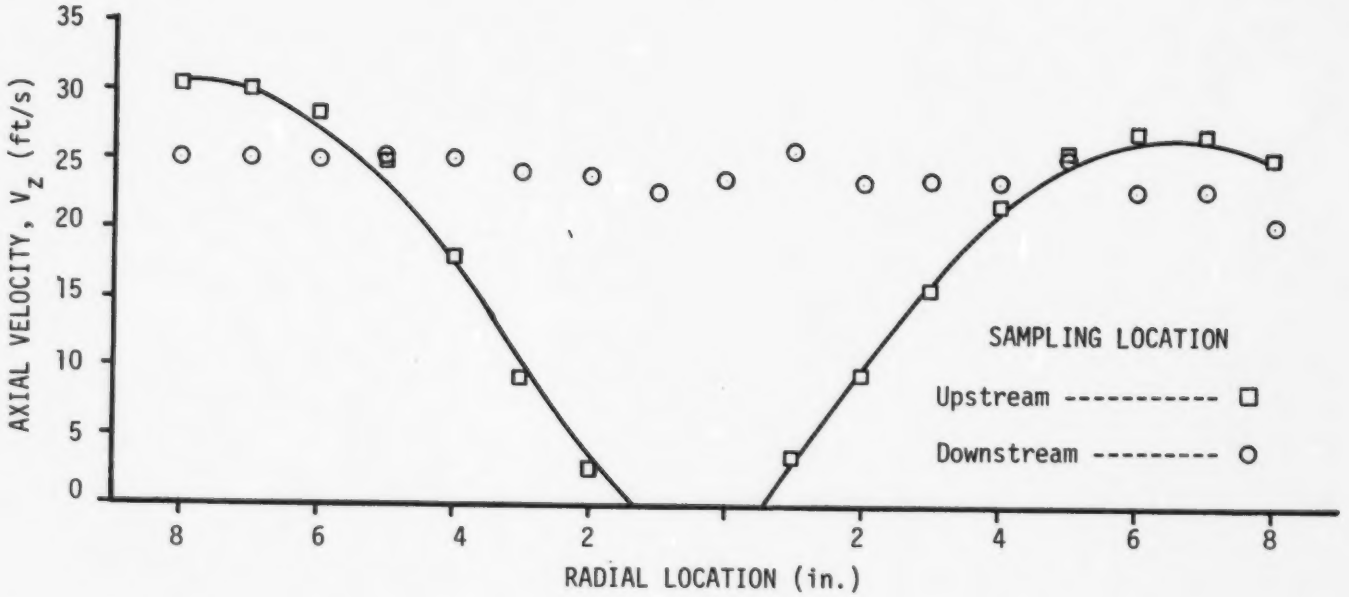

Figure 53. V_z vs. location of a D/6 egg crate flow straightener (length = 3 in.; Q = 40 ft^3/s)

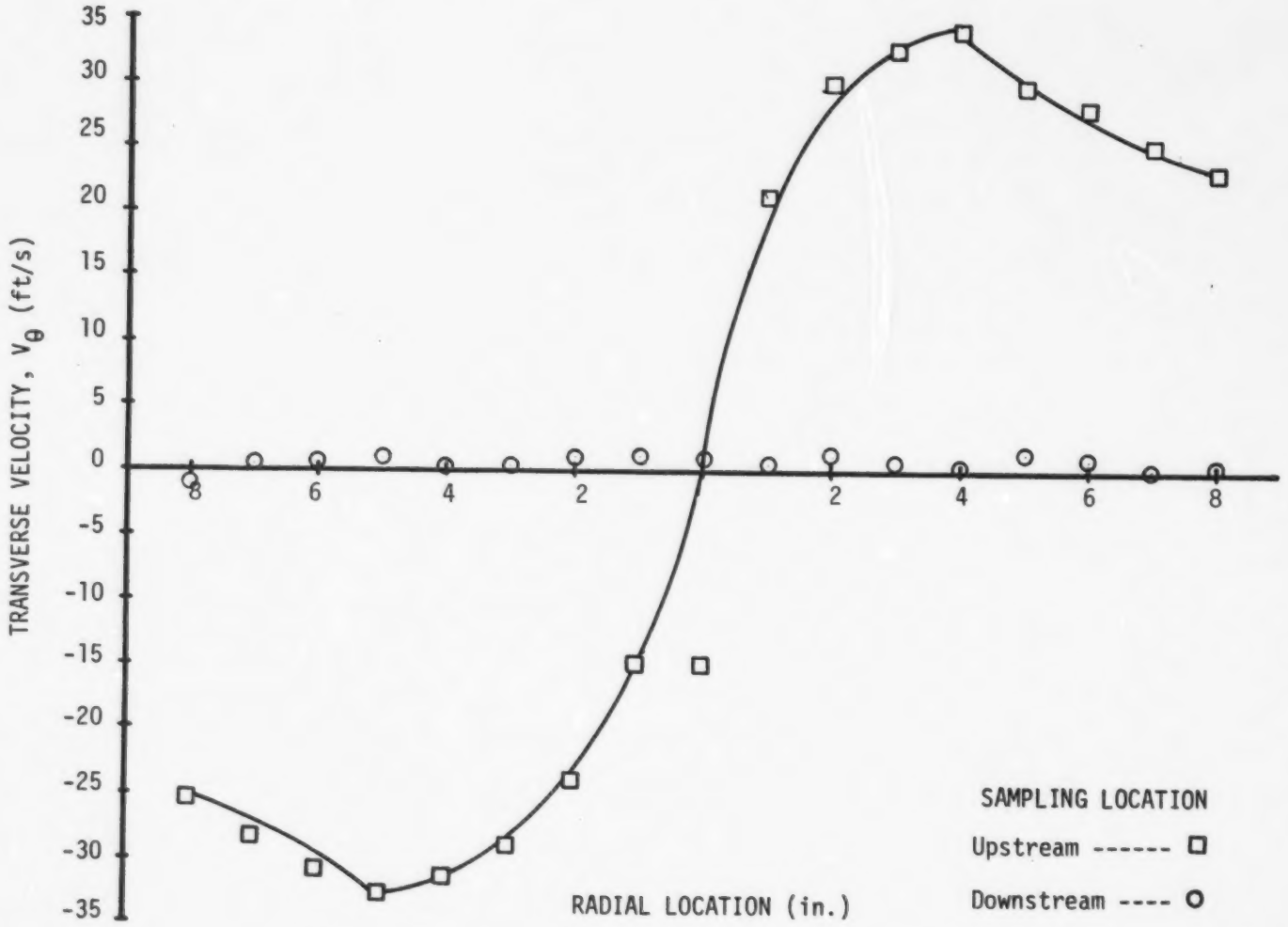

Figure 54. V_θ vs. location of a D/6 egg crate flow straightener (length = 3 in.; Q = 40 ft^3/s).

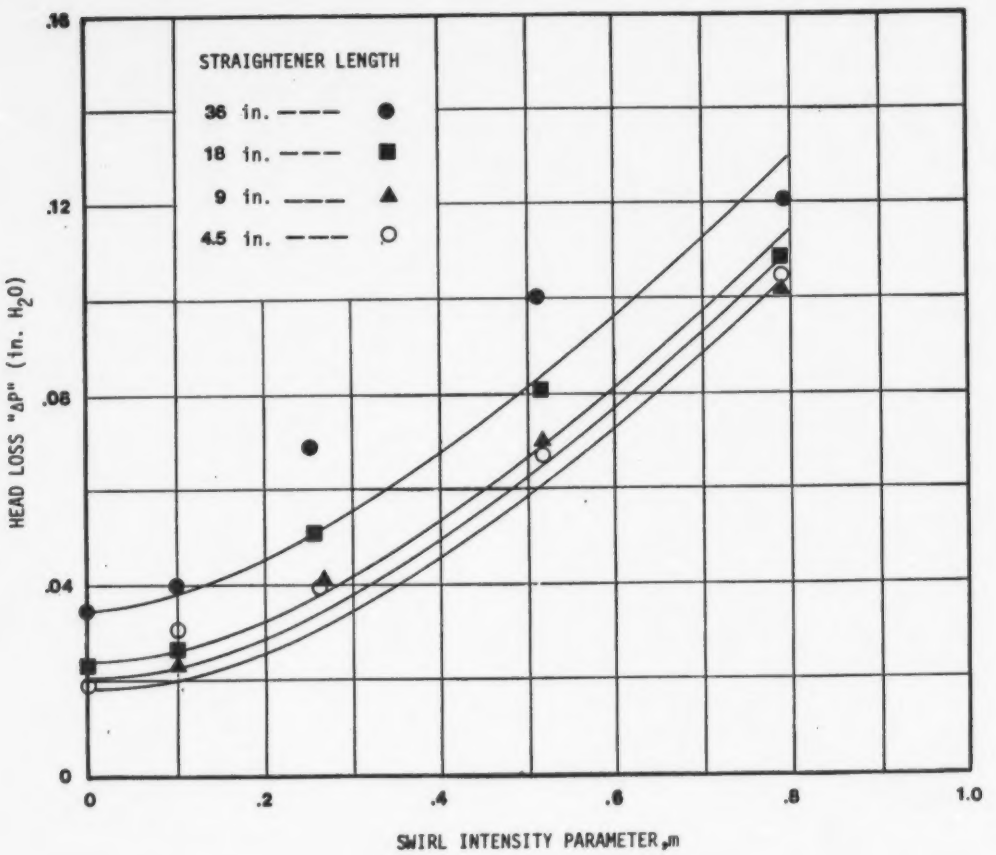

Figure 55. Head loss vs. swirl intensity for egg crate-type flow straightener of cell size c = 4 1/2 in. (flow rate = 40 ft^3/s).

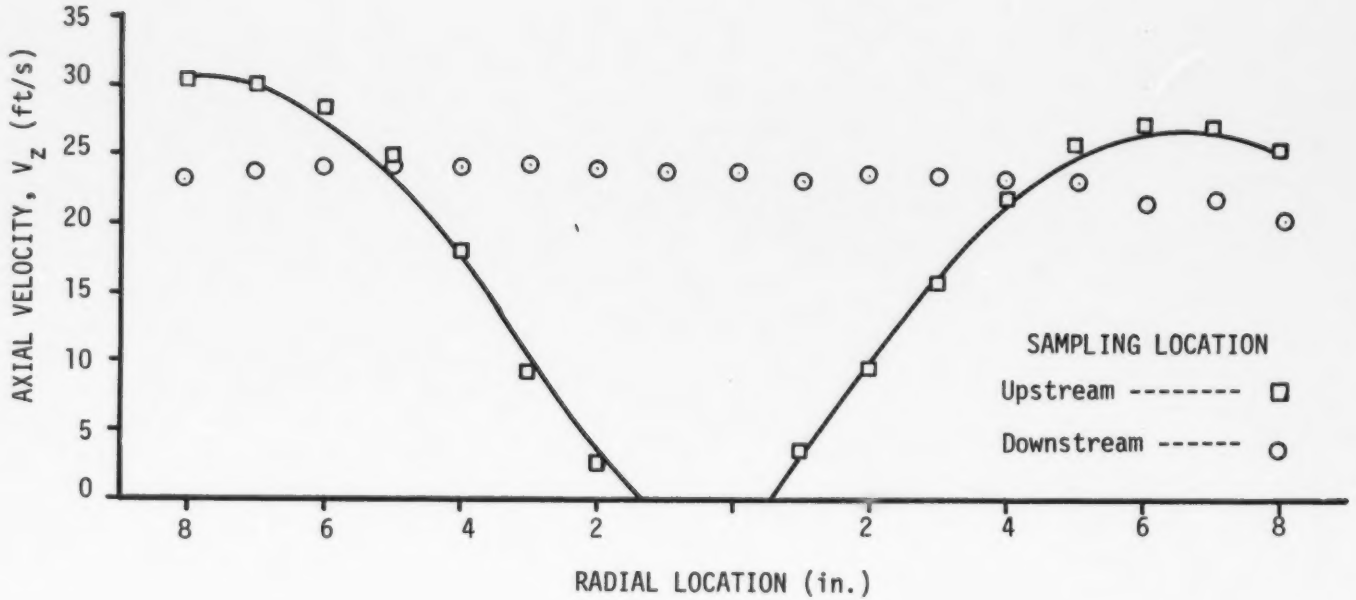

Figure 56. V_z vs. location of a D/4 egg crate flow straightener (length = 4 1/2 in.; Q = 40 ft^3/s).

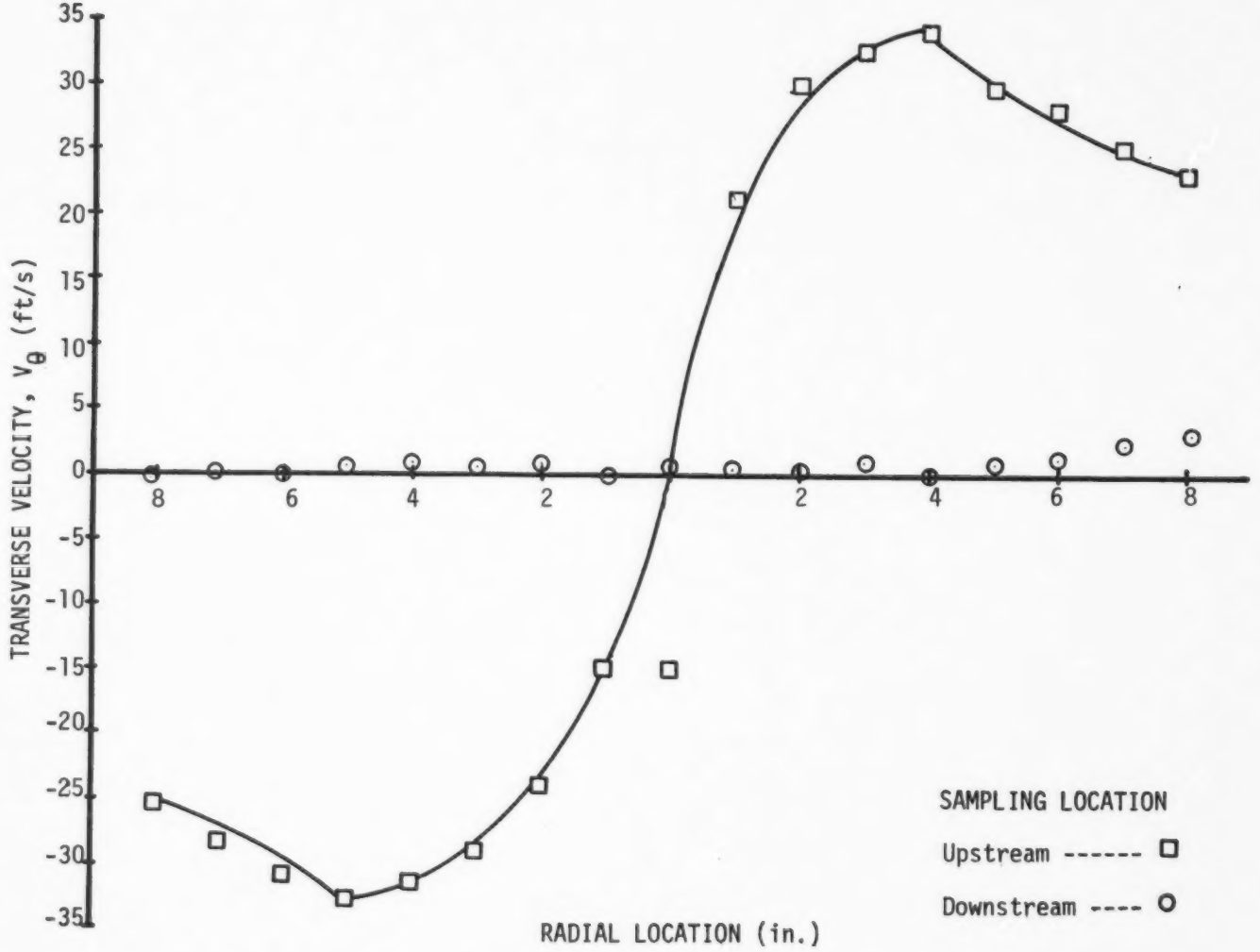

Figure 57. V_θ vs. location of a D/4 egg crate flow straightener (length = 4 1/2 in.; Q = 40 ft^3/s).

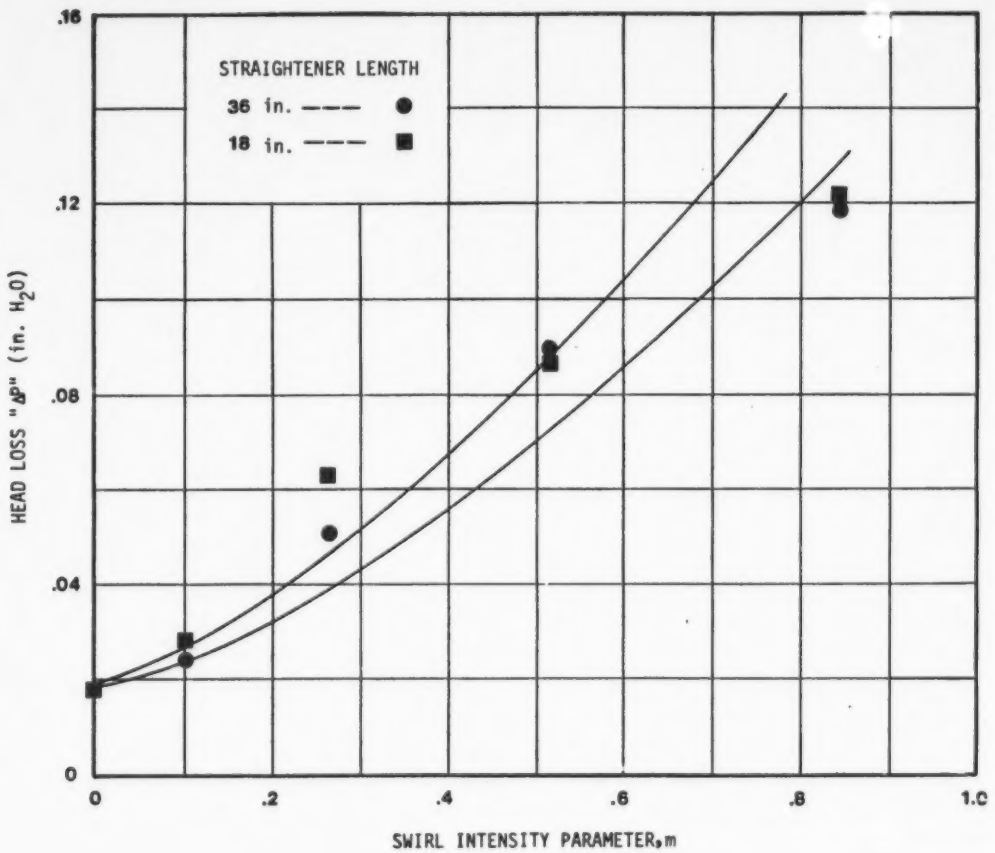

Figure 58. Head loss vs. swirl intensity for a 4-vane étoile-type flow straightener (flow rate = 40 ft^3/s).

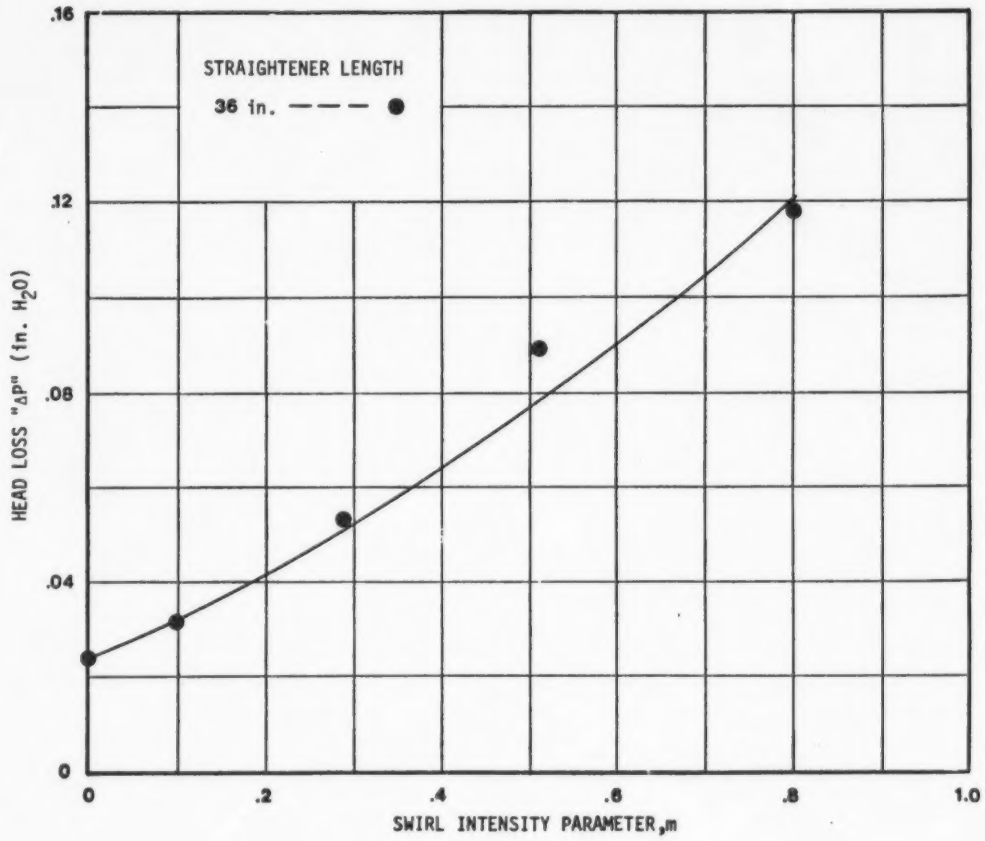

Figure 59. Head loss vs. swirl intensity for an 8-vane étoile flow straightener (flow rate = 40 ft^3/s, straightener length = 36 in.).

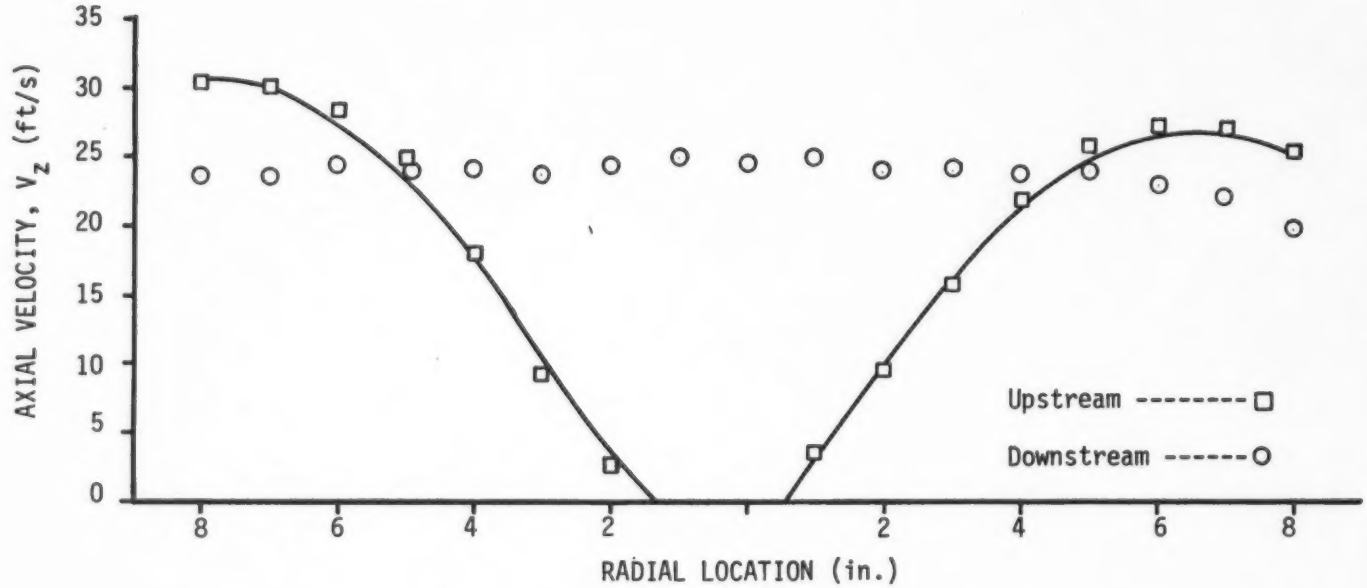

Figure 60. V_z vs. location 4-vane étoile flow straightener (length 18 in.; Q = 40 ft^3/s).

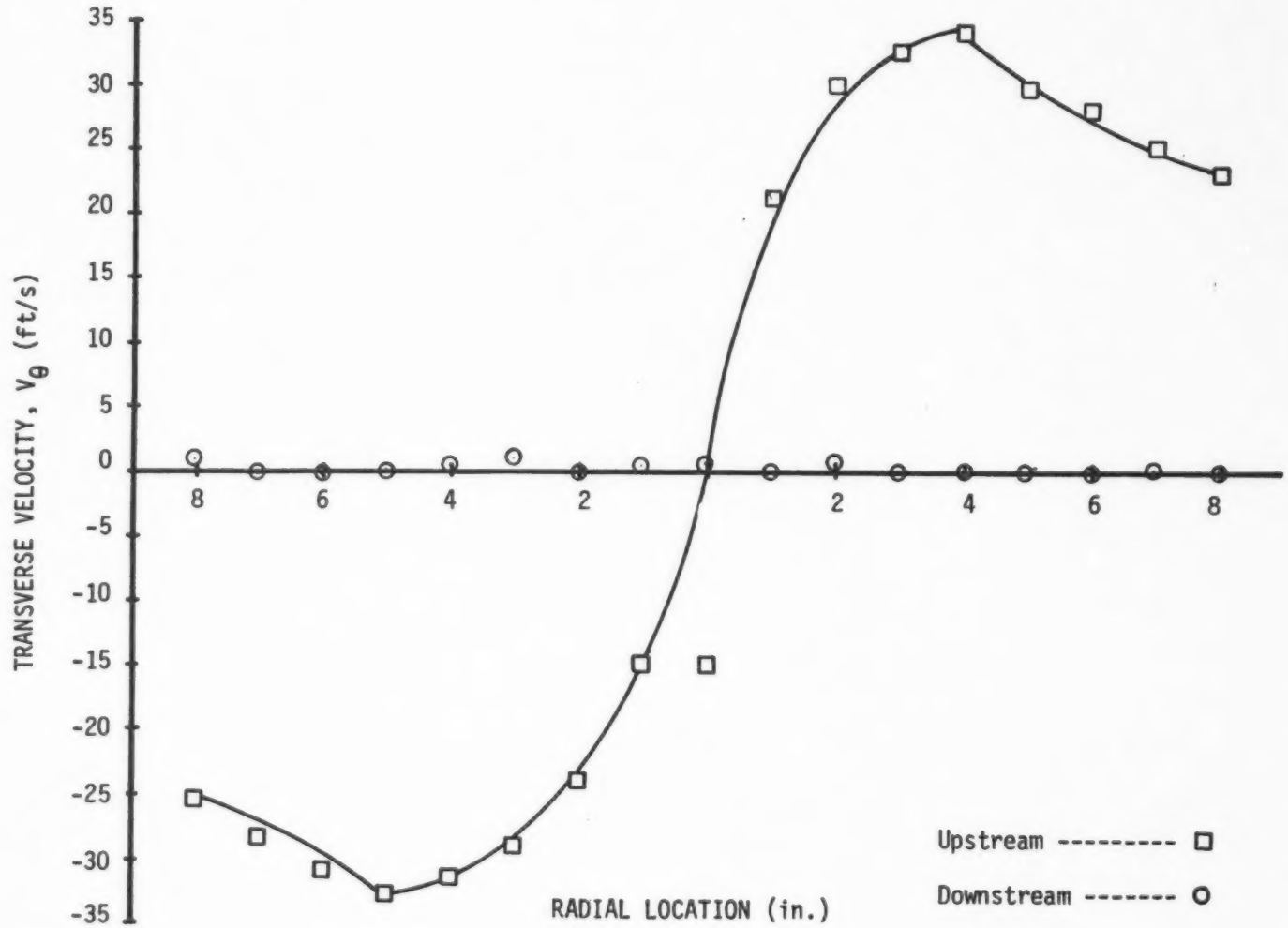

Figure 61. V_θ vs. location 4-vane étoile flow straightener (length = 18 in.; Q = 40 ft^3/s).

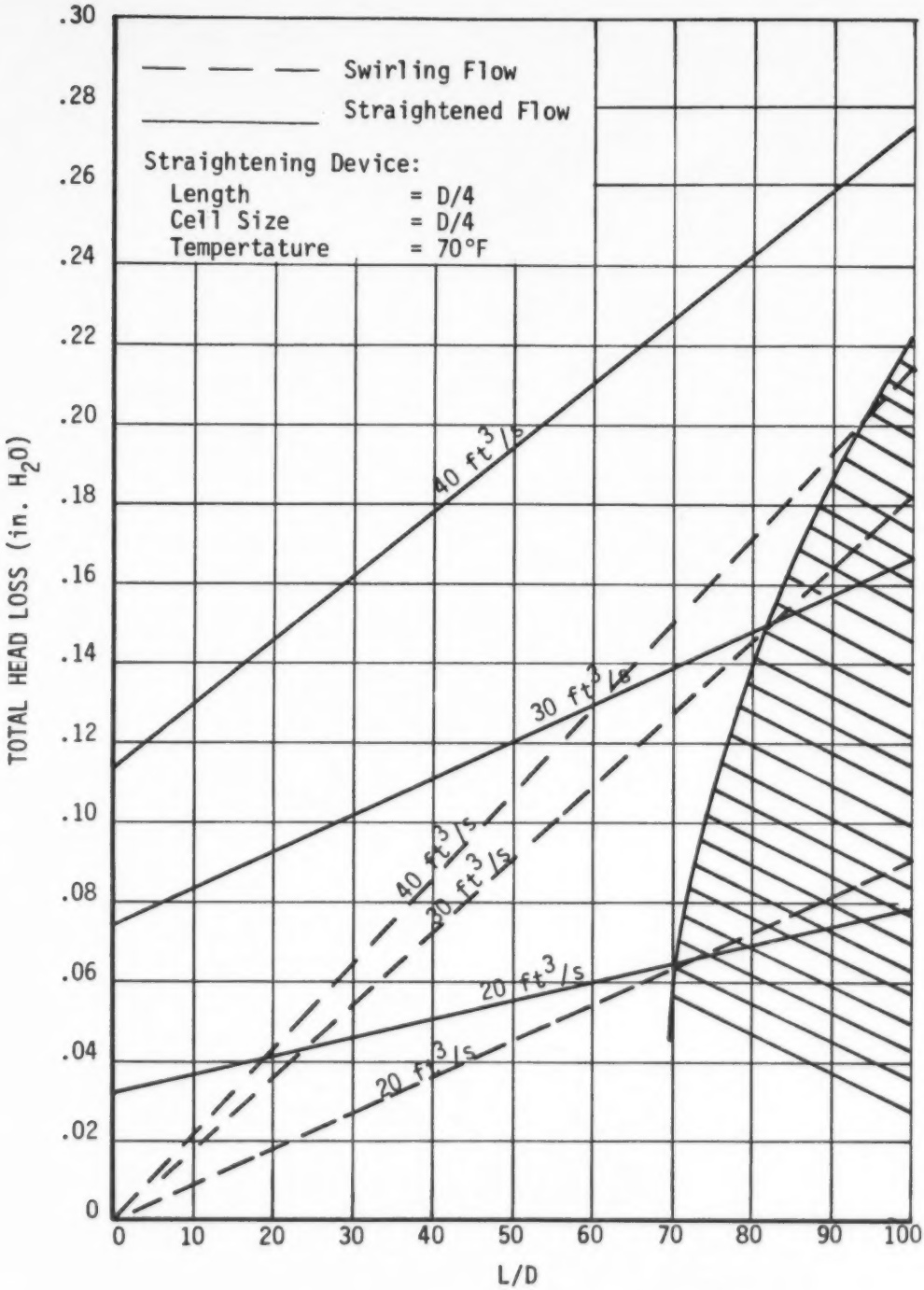

Figure 62. Total head loss vs. stack L/D for straightened flow and swirling flow.

TABLE 1. CORE VELOCITY PROFILE AT THROAT

ξ_2	V'_{z2}	$\xi V'_{z2}$
0	1.0809	0
0.1	1.0810	0.10810
0.2	1.0794	0.2159
0.3	1.0760	0.3228
0.4	1.0708	0.4283
0.5	1.0638	0.5319
0.6	1.0549	0.6329
0.7	1.0442	0.7309
0.8	1.0315	0.8252
0.9	1.0168	0.9151
1.0	1.0000	1.0000

TABLE 2. EXPERIMENTAL RESULTS

RUN NUMBER	m	Q_{actual} NO SWIRL (INLET VENT.)	Q_{actual} SWIRL (TEST VENT.)	C_D
1	0.261	20.80	21.69	0.96
2	0.321	35.02	34.57	1.01
3	0.323	35.02	34.43	1.02
4	0.334	25.02	34.01	1.03
5	0.399	25.55	25.83	0.99
6	0.436	35.02	34.33	1.02
7	0.456	20.44	20.89	0.98
8	0.555	35.02	34.57	1.01
9	0.563	20.51	21.42	0.96
10	0.572	19.07	22.38	0.85
11	0.589	35.02	34.211	1.02
12	0.625	19.07	21.89	0.87
13	0.724	35.02	39.04	0.90
14	0.783	35.02	40.31	0.87
15	0.802	19.07	23.67	0.81
16	0.874	35.02	41.41	0.85
17	0.883	35.02	41.15	0.85
18	0.906	19.07	24.36	0.78
19	0.968	19.07	25.50	0.75
20	0.977	18.62	25.83	0.72
21	0.988	10.33	20.89	0.49
22	1.011	19.07	25.68	0.74
23	1.024	20.97	24.94	0.84
24	1.030	19.85	25.96	0.77
25	1.078	16.86	25.21	0.67
26	1.107	28.62	36.12	0.79

TABLE 3. SWIRL GENERATOR CALIBRATION

FLOW RATE (ft^3/s)	SWIRL INTENSITY, m	ROD LENGTH (in.)[a]
20	0	7
20	0.103444	18
20	0.241443	20
20	0.574567	22
20	0.859228	24
30	0	7
30	0.096039	18
30	0.310646	20
30	0.566211	22
30	0.808553	24
40	0	7
40	0.095958	18
40	0.268077	20
40	0.521217	22
40	0.797256	24

[a] This dimension is measured from the side of the swirl generator box to the outside of the end nut.

TABLE 4. YAW ANGLES VERSUS TRAVERSE POINT[a]

Distance from Stack Wall (in)	Yaw Angle Port A (θ)	Yaw Angle Port B (θ)
1	46	45
3	52	47
5	58	50
7	65	50
9	68	53
11	57	56
13	0	58
15	-54	-1
17	-52	-45
19	-46	-44
21	-40	-41
23	-34	-37
25	-28	-37
27	-20	-32
29	-20	-26

[a] Data taken about 25 ft. downstream from water spray chamber exit.

TABLE 5. COMPARISON OF PARTICULATE CONCENTRATIONS AND VOLUMETRIC FLOW UPSTREAM AND DOWNSTREAM FROM THE EGG CRATE STRAIGHTENER

RUN NUMBER	CONCENTRATION (gr/dscft)		VOLUMETRIC FLOW (ft^3/min)	
	UPSTREAM	DOWNSTREAM	UPSTREAM	DOWNSTREAM
1	0.059	0.059	4850	4425
2	0.067	0.070	4885	4250
3	0.012	0.010	4070	4070
AVERAGE	0.046	0.046	4600	4250
4	0.010	0.0082		
5	0.014	0.014		
6	0.047	0.039		
7	0.016	0.015		
8	0.029	0.025		
AVERAGE	0.023	0.020		

REFERENCES

1. Mitchell, W.J., B.E. Blagun, D.E. Johnson, and M.R. Midgett. Angular Flow Insensitive Pitot Tube Suitable for Use With Standard Stack Testing Equipment. EPA 600/4-79-042, U.S. Environmental Protection Agency, Research Triangle Park, North Carolina, 1979. 79 pp.

2. Senoo, T., and T. Nagata. Swirl Flow in Long Pipes with Different Roughness. Bulletin of J.S.M.E., 15(90), 1972.

3. Fox, R.W., and A.T. McDonald. Introduction to Fluid Mechanics, Second Edition. John Wiley and Sons, New York, New York, 1973, 684 pp.

4. Idelchik, I.E. Handbook of Hydraulic Resistance; Coefficients of Local Resistance and of Friction. Israel Program for Scientific Translations, Jerusalem, 1966. 517 pp.

5. Massey, B.S. Mechanics of Fluids. Van Nostrand Reinhold Company, New York, New York, 1970.

6. Sabersky, R.H., and A.J. Acosta. Fluid Flow - A First Course in Fluid Mechanics. The Macmillan Company, New York, New York, 1964.

7. Murakami, M., and O. Kito. Effects of Swirling Flow Component on Discharge Coefficients of Constriction Meters (in case of orifice). Bulletin of J.S.M.E., 21(151), 1978.

8. Barkley, T., Effects of Swirling Flow on the Accuracy of Venturi Flow Meters. Senior Thesis, Mechanical Engineering Department, Auburn University, Auburn, Alabama, 1979.

9. Goerner, C.L., F.H. Hartman, and J.B. Draper. A Method for Stack Sampling Cyclonic Flow. Paper 78-35.2. Presented at the National Conference of Air Pollution Control Association, Houston, Texas, June 25-30, 1978.

10. Peeler, J.W., F. Phoenix, and D.J. Grove, Characterization of Cyclonic Flow and Analysis of Particulate Sampling Approaches at Asphalt Plants. Entropy Environmentalists, Inc., Research Triangle Park, North Carolina.

11. Durham, M.D. Isokinetic Sampling of Aerosols From Tangential Flow Streams. Dissertation. University of Florida, Gainesville, Florida 1978.

12. Spencer, E.A., Developments in Industrial Flowmetering. Chemical and Process Engineering, January 1963.

13. Bonnington, S.T. and Zanker, K.J., Flow Measurement Errors. Chemical and Process Engineering, December 1960.

14. Sprenkle, R.E. and N.S. Courtright, Straightening Vanes for Flow Measurement, Mechanical Engineering, February 1958.

15. Kinghorn, F.C., A. McHorn, and W.D. Dyet, The use of E'toile Flow Straighteners with Orifice Plates in Swirling Flow, A.S.M.E. Winter Annual Meeting, 1979 No. 79-WA/FM-7, National Engineering Laboratory, East Kibride Glasgow, Scotland.

APPENDIX A

DESIGN AND CALIBRATION OF THE INLET VENTURI

DESIGN

The inlet venturi, shown in Figure 6, was designed as a flow measuring device to monitor the rate of flow into the test section of the experiemental facility.

A basic duct diameter of 19 in. was chosen to match the suction side fan opening and an overall length of 18 ft. was selected to fit the available work area. The throat diameter needed to be of a size that would produce a manometer reading of 5 in. H_2O at an inlet velocity of 60 ft^3/s. This diameter was calculated to be 12.29 in., but for greater clarity and uniformity the throat diameter was scaled down to an even 12 in. In alignment with the ideal model [5], a total included angle of 22° was chosen for the converging section and a total included angle of 8° was chosen for the diffuser section.

The six, equally spaced, high pressure taps were placed in accordance with the ideal model [6], but the six low pressure taps were moved 2 in. downstream from the ideal model location. This change was made to allow the air flow to rejoin the wall (if separation occurred), since the nozzle was constructed from sheet metal and not cast from an uncut mold.

According to the ideal model, 10 pipe diameters of duct should precede the venturi; however, the available work area would only permit a 5-diameter approach. To compensate for this revision, two devices were added - air straighteners and a conical regulator.

The air straighteners were fabricated from short cardboard tubes which were glued together and inserted at each end of the nozzle. The conical regulator was placed on adjustable slides to allow flow regulation and to allow the air to enter the duct in a more uniform manner.

Listed below are the design dimensions for the inlet side of the test facility:

Cone:	2 ft. in diameter, 45°
Intake Section of Nozzle:	7.5 ft. in length 1.58 ft. in diameter
Converging Section of Nozzle:	1.5 ft. in length 22° angle
Throat Section of Nozzle:	1 ft. in length 1 ft. in diameter
Diverging Section of Nozzle:	4.17 ft. in length 8° angle
Exit Section of Nozzle:	3.0 ft. in length 1.58 ft. in diameter

CALIBRATION

The calibration was performed in the venturi throat which, for sampling purposes, was divided into five circular regions of equal area. The inlet cone was set and a pitot tube was inserted into the venturi throat and traversed across a diameter, sampling at ten locations, two per area. Five traverses were then made at this cone setting and the data for each point were averaged. These averaged values were then used to compute the actual flow rate (Q_{actual}).

The pressure signal was then taken across the inlet venturi and an ideal venturi flow rate was calculated (Q_{ideal}).

The venturi discharge coefficient (C_v) was then calculated using

$$Q_{actual} = C_v \, Q_{ideal}$$

This process was then repeated for ten different inlet cone settings and the results are shown in Figure A-1.

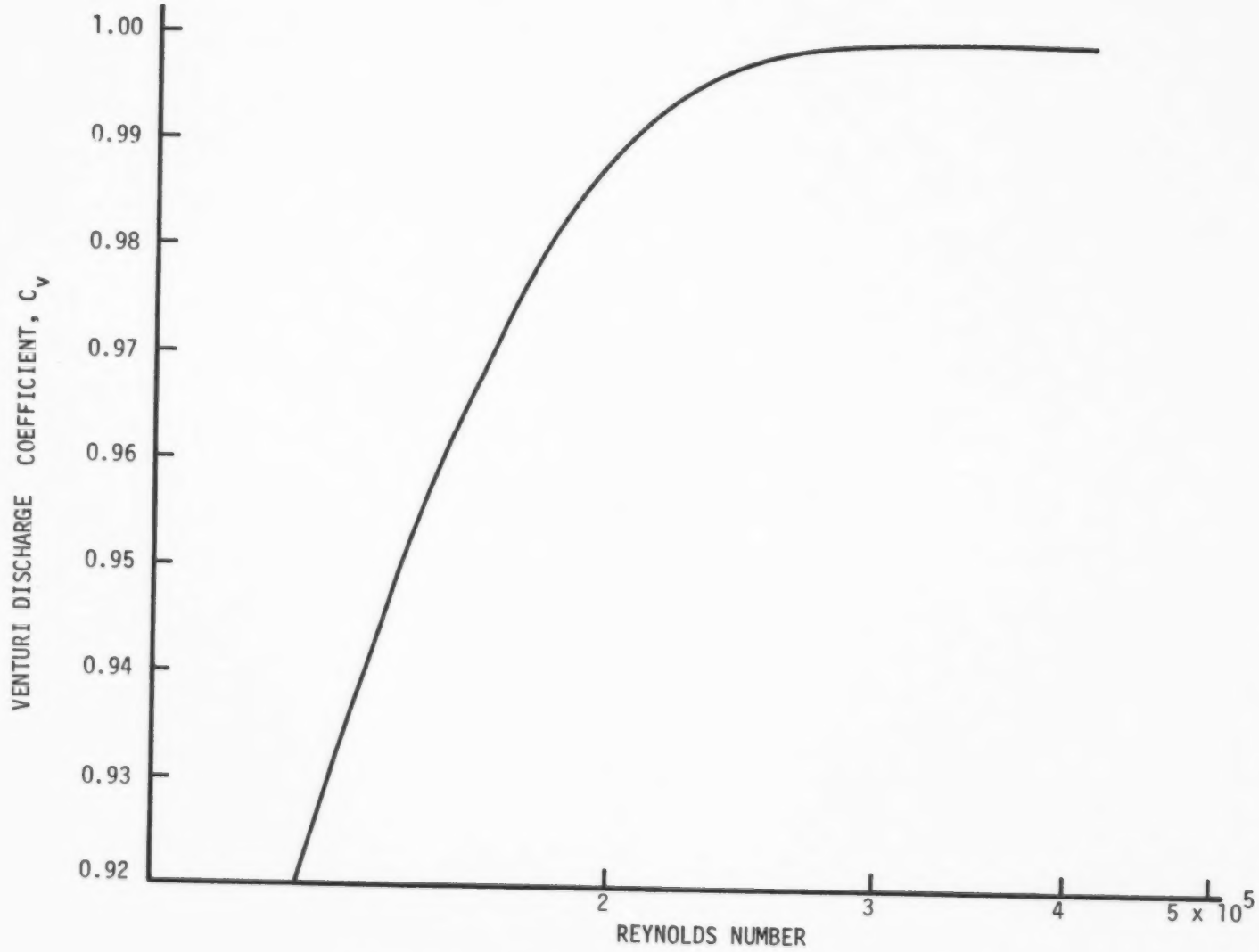

Figure A-1. Discharge coefficient curve for inlet venturi.